Investigating Short-Wavelength Correlated Errors on Low-Resolution Mode Altimetry

G. DIBARBOURE

Collecte Localisation Satellite, Ramonville St-Agne, France

F. BOY AND J. D. DESJONQUERES

Centre National d'Etudes Spatiales, Toulouse, France

S. LABROUE AND Y. LASNE

Collecte Localisation Satellite, Ramonville St-Agne, France

N. PICOT

Centre National d'Etudes Spatiales, Toulouse, France

J. C. POISSON AND P. THIBAUT

Collecte Localisation Satellite, Ramonville St-Agne, France

(Manuscript received 18 April 2013, in final form 7 January 2014)

ABSTRACT

The observation of ocean scales smaller than 100 km with low-resolution mode (LRM) altimetry products is degraded by the existence of a ''hump artifact'' visible on sea surface height (SSH) spectra.

Through an analysis of simulations and actual data from multiple missions, this paper shows that the hump originates in a response to inhomogeneities in backscatter strength. Current retrackers cannot fit their Brown model properly because they were designed for a scene with homogeneous backscatter properties. The error is also smoothed along track because of the size and shape of the LRM disc-shaped footprint. Therefore, the hump is modulated by the altimeter design and altitude and by the retracker used.

Because of the random nature of the phenomenon, a large majority of long topography segments (e.g., hundreds to thousands of kilometers) is affected. However, within these segments, a substantial fraction of the corruption is contained in small subsets of data (e.g., less than 10%). This paper shows that oceanography users interested in small-scale SSH signals can mitigate the hump corruption by using better editing and postprocessing algorithms on the 20-Hz rate of current products.

Last, the thin stripe-shaped footprint of *Cryosat-2*'s synthetic aperture radar mode (SARM) is not affected by the hump artifact, thus improving the observation of topography features ranging from 30 to 100 km. The differences between SARM and pseudo-LRM sigma0 can also be used to detect major hump events on pseudo-LRM data, which might be an asset to design/validate a new generation of algorithms aimed at reducing the hump artifact on the existing LRM record.

1. Introduction

a. Context and objectives

Satellite radar altimetry is used to observe a wide range of spatial scales, ranging from basin scale to small mesoscale, that is, less than 100 km. For multialtimeter maps [e.g., Archiving, Validation, and Interpretation of Satellite Oceanographic data (AVISO)/ Data Unification and Altimeter Combination System (DUACS) from Le Traon et al. 2003; Dibarboure et al. 2011] the main limitation is in the cross-track direction, and it stems from the number of satellites in the constellation (e.g., Chelton and Schlax 2003; Le Traon and Dibarboure 2002). To analyze scales smaller than 150 km, one must use along-track altimetry

Corresponding author address: Gerald Dibarboure, Space Oceanography Division, Collecte Localisation Satellites, 8-10 Rue Hermès, Parc Technologique du Canal, 31520 Ramonville Saint-Agne, France.
E-mail: gerald.dibarboure@cls.fr

DOI: 10.1175/JTECH-D-13-00081.1

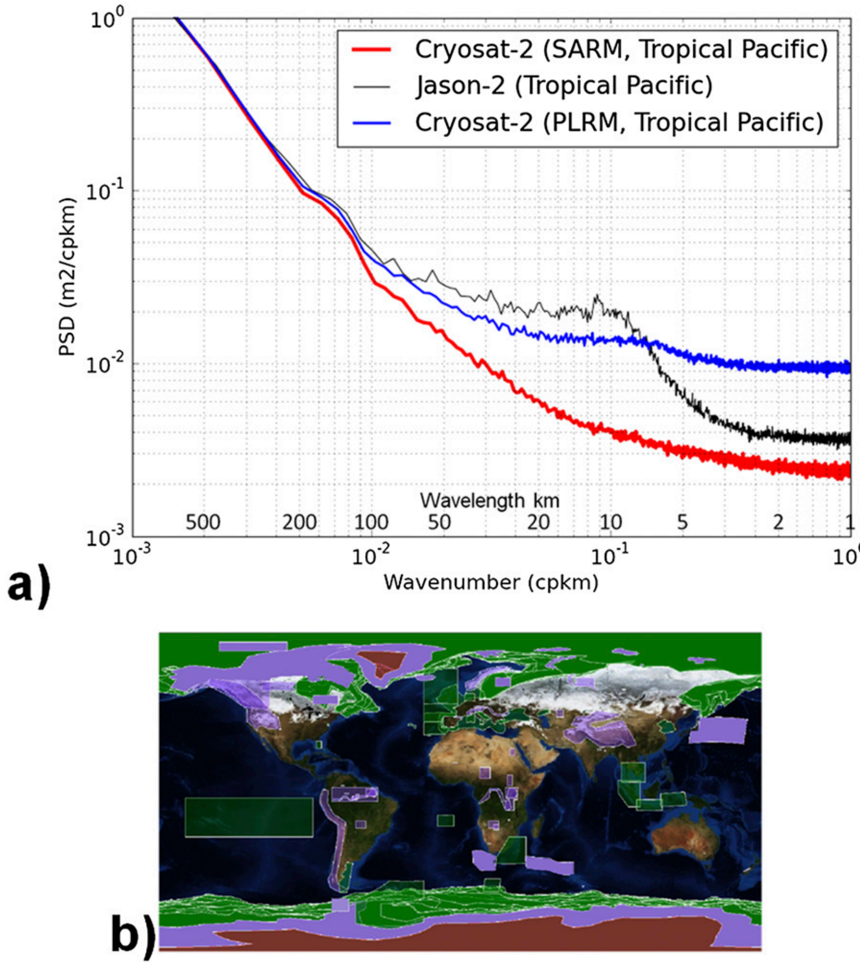

FIG. 1. (a) Mean SSH anomaly spectrum from *Jason-2* (black), Cryosat pseudo-LRM (blue), and Cryosat SAR (red). No geophysical correction applied, precise orbit ephemeris (POE) solutions used, same geographical selection for all datasets [green SARM acquisition box in the tropical Pacific Ocean; see (b)], and same period for all missions (May–June 2012, i.e., *Jason-2* cycles 141–146). (b) *Cryosat-2* mode acquisition mask (as of January 2013) with SARM in green, SARin in purple, and LRM elsewhere.

products, such as the Geophysical Data Record (GDR).

Along-track GDR products have a resolution as small as 300 m (20-Hz rate), although the resolution most commonly used in oceanography is 6–7 km (1-Hz rate). For these products, the main limitation to observing small mesoscale is the error level of the sea surface height (SSH). Indeed, the ''noise'' observed on 1-Hz products is of the order of 3 cm on Jason-class missions (Ablain et al. 2010).

Because the sea level anomaly (SLA) power spectral density (PSD) decreases with wavenumber (e.g., Scott and Wang 2005), the 3-cm Gaussian noise (i.e., flat power spectrum) can corrupt wavelengths as large as 100 km (Kim et al. 2011). Although altimeters *can* observe smaller mesoscale features concurrently with other remote sensing sensors when the signal-to-error ratio is favorable (e.g., Birol et al. 2010; Dussurget et al. 2011), high wavenumber errors remain the main limiting factor (Xu and Fu 2012).

In this context, the 3-cm noise of 1-Hz data should be compared to the 20-Hz instrumental noise of the order of 7–9 cm on Jason-class altimeters. Both error levels are not linked by the factor sqrt(20) as one would expect if the error was Gaussian. This is explained by the black curve in Fig. 1 [derived from Boy et al. (2012); processing and data detailed in section 4e]. This PSD shows that the flat Gaussian plateau is reached only for wavelengths smaller than a few kilometers. The 3-cm error seen as a Gaussian plateau on 1-Hz data actually comes from a spectral ''hump'' affecting the PSD from 3 to 100 km. This spectral hump is the main contributor to the small-scale error of Jason-class missions, as discussed by Faugère et al. (2006).

In this paper we analyze instrumental simulations (section 2) and actual data from various altimetry missions (section 3) to investigate the origin and the properties of the spectral hump observed on Jason-class missions, that is, low-resolution mode (or LRM) altimetry. In section 4, we discuss potential improvements to detect and/or to reduce the spectral hump on existing products, as well as observations from recent synthetic aperture radar mode (SARM) datasets from *Cryosat-2*.

b. Terminology

In this study, we make extensive use of the notion of altimeter footprint. We focus on two specific footprints: the LRM *waveform footprint*—that is, the disc-shaped surface of the sea that is illuminated to create the altimeter waveform (its radius is approximately 10 km for *Jason-2* and 7 km for *Cryosat-2* LRM); and the *leading-edge footprint*—that is, the surface of the sea that is illuminated when the backscattered energy increases on the first nonzero waveform gates (of the order of 1–3 km on *Jason-2*). This definition is consistent with the retracking process used on Jason-class missions, *Cryosat-2* LRM, or the *Environmental Satellite* (*Envisat*) and the European Sensing Satellite (ERS) (e.g., Amarouche et al. 2004; Thibaut et al. 2010).

Chelton et al. (2001) and Hayne (1980) also describe how the leading-edge footprint has a geometry and size that change with crest through wave height (e.g., of the order of 1–3 km for significant wave height ranging from 1 to 10 m), whereas the waveform footprint does not.

Note that these definitions are different from the notion of pulse-limited footprint defined for Ocean Topography Experiment (TOPEX) by Chelton et al. (2001), since the latter is associated with *only one* waveform gate (one annulus, not the entire disc). The waveform footprint is also different from the beam-limited footprint, defined as the area within the field of view of the antenna gain pattern (approximately 15 km for *Jason-2*), as the latter is not necessarily in the waveform.

Cryosat-2 has a slightly elliptical antenna: the 3-dB beamwidth is 1.08° in the along-track direction and 1.2° in the across-track direction (i.e., 6.7 km × 7.4 km). Yet, the LRM footprint is considered circular here, since we use the approximation from Wingham and Wallis (2010).

In the case of SARM data from *Cryosat-2*, the delay Doppler process described by Raney (1998) creates a synthetic footprint, that is, a small stripe of the order of 300 m in the along-track direction and as large as the LRM waveform footprint in the across-track direction (Fig. 2).

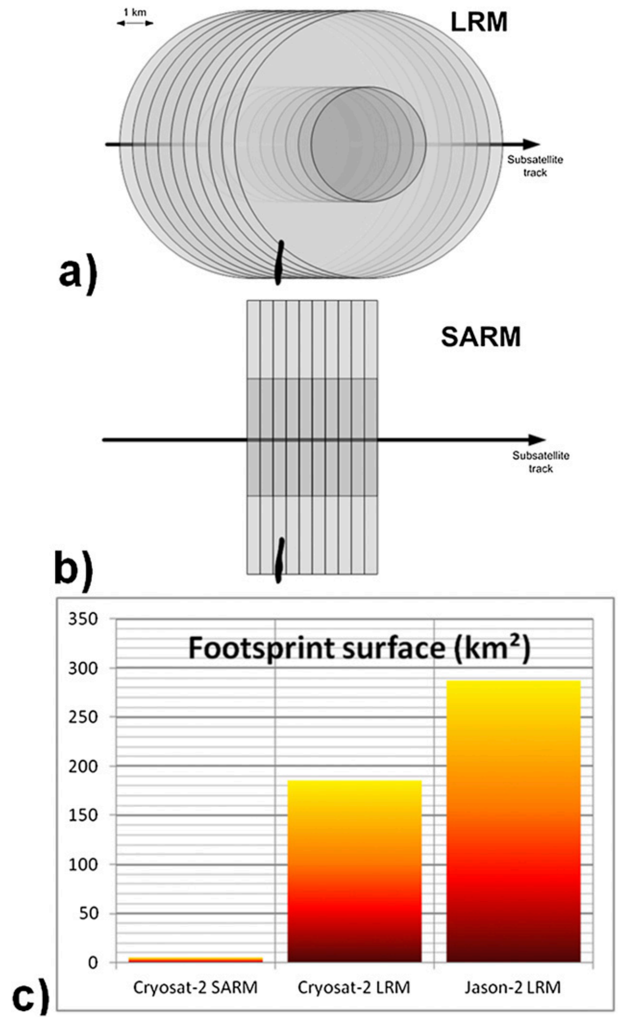

FIG. 2. Altimeter footprint geometry on a 3-km segment for (a) LRM and (b) SARM. Darker zones highlight the leading-edge footprint, providing the bulk of the SSH content through the leading edge of the waveform. The tiny black shape at the bottom of each subplot illustrates how a single SARM footprint (i.e., waveform) can be affected by isolated spurious reflections, whereas larger LRM footprints repeatedly sample the error over multiple waveforms (i.e., correlated error). (c) Surface of the altimeter footprint (km^2) or the traditional and SAR modes of *CryoSat-2* and *Jason-2*.

c. The Brown model

Most retrackers used on current ground processors are using a model derived from Brown (1977), where the altimeter waveforms are the result of a double convolution: WF = FSSR × IR × PDF. Here, FSSR is the flat sea surface response, IR is the impulse response of the altimeter, and PDF is the probability density function of surface elevation due to wave height.

There are two notable assumptions made when using a Brown model: 1) the surface height statistics are assumed to be constant over the total area illuminated by the radar during construction of the main return; and 2) the backscattering process is only a function of the reflection angle, antenna pattern, and sigma0 (i.e., homogeneous backscattering scene in the waveform footprint), and the PDF is homogeneous in the scene.

Note that whether the scene in the footprint is homogeneous or not, the retracked LRM waveform is always obtained from the stacking of coherent echoes acquired at the instrument's pulse repetition frequency (PRF).

2. Theoretical simulations

a. Introduction and methodology

In this section, we analyze the output of a simple SARM and LRM simulator, using the range and Doppler domain derived from Raney (1998). The simulation is performed on a SARM Doppler geometry (Fig. 2b) with a numerical convolution of the FSSR, IR, and PDF parameters. The FSSR is computed on the radar footprint, that is, a 7-km disc for *Cryosat-2* LRM (Fig. 2a) using reflections from a grid of 50 cm $\times$ 50 cm cells. The power received is then integrated as an FSSR amplitude in the range (47-cm resolution) and Doppler (300-m resolution) domain. This FSSR matrix is then convolved with an instrumental IR (Doppler and range) and PDF (range domain, once for each Doppler band). The result is a matrix of single-look echoes for each Doppler band (i.e., synthetic aperture footprint, 300 m $\times$ 8 km, as per Fig. 2b). The matrix is computed at 20 Hz.

From this matrix, we either use synthetic aperture radar processing to generate 20-Hz SARM-simulated data on each synthetic aperture footprint, or we simply sum all Doppler bands to generate 20-Hz LRM waveforms on the entire LRM waveform footprint. For the sake of simplicity, the simulations presented in this paper do not contain any speckle noise (i.e., the true instrumental white noise observed from 600 m to 3 km on the black spectrum from Fig. 1), and sensitivity studies show no influence of this noise on our conclusions.

b. Singular corrupted pixel

The spectral hump of LRM data (Fig. 1, black) exhibits a transition to instrumental white noise between 3 and 10 km. The former is the radius of the leading-edge footprint, shown as smaller and darker discs in Fig. 2a; and the latter is the size of the radius of the waveform footprint (i.e., the larger and lighter discs from Fig. 2a).

We therefore assume that the LRM footprint artificially smoothes the altimeter response to the presence of spurious pixels on the surface: the small black zone at the bottom of Fig. 2a and Fig. 2b indeed shows that a small region with different backscatter characteristics will be sampled repeatedly in the LRM footprint but not in the SARM footprint.

To understand the influence of the LRM smoothing, we perform a simulation using a realistic SSH [output of the very high-resolution ocean model from Klein et al. (2008)], and constant sigma0 and significant wave height (SWH) values in a 300-km-long scene. Then we artificially increase the sigma0 value of a single Doppler band (300 m along track $\times$ 8 km across track) by 3 dB: we study the LRM altimeter's response to a high radar return cross section, commonly called a sigma0 bloom (e.g., Mitchum et al. 2004; Thibaut et al. 2010). In our simulation, the bloom is limited to a very small zone of the ocean (i.e., a Dirac with respect to the altimeter resolution). While the approach is simpler than the circular-patch model developed by Tournadre et al. (2006), or the simulations with square facets from Quartly (1998), the principle is the same.

Figures 3a and 3c show how LRM waveforms are corrupted by the presence of this singular +3-dB value: the parabolic migration is clearly visible and consistent with observations on actual data: both in coastal areas (Gómez-Enri et al. 2010; Quartly 2011) and in the open ocean from specular reflection sources, such as ocean slicks, ships, or icebergs (Tournadre et al. 2006; Tournadre 2007; Tournadre et al. 2008).

Figures 3b and 3d show the simulated (black) and retracked (red) SLA values around the corrupted sigma0 pixel. In these plots, we use a maximum likelihood estimator 4 (MLE4) retracker similar to the algorithms used for *Jason-2* GDR products and based on a Brown model that assumes that the backscattering parameters are constant in the scene, that is, unable to account for the spurious +3-dB value.

The retracked response to the sigma0 Dirac is a spatially coherent and sinc-like SLA error affecting a 15-km band around the corrupted pixel (the amplitude of 15 cm is linked with the arbitrary +3-dB offset used on our bloom source). The same type of spatially coherent errors can be observed on all retracked parameters (not shown), as expected from the correlation between MLE-retracked parameters (Challenor and Srokosz 1989; Sandwell and Smith 2005; Rodriguez et al. 2007).

The largest errors are observed in the 3-km window, where the sigma0 bloom reaches the leading-edge footprint because the bulk of the retracked SSH content is contained in the waveform leading edge. Yet, the SSH is corrupted even 7 km away from the bloom source because the retracker projects a fraction of the parabolic signature back into the retracked position and slope of the leading edge (discussed in section 4d).

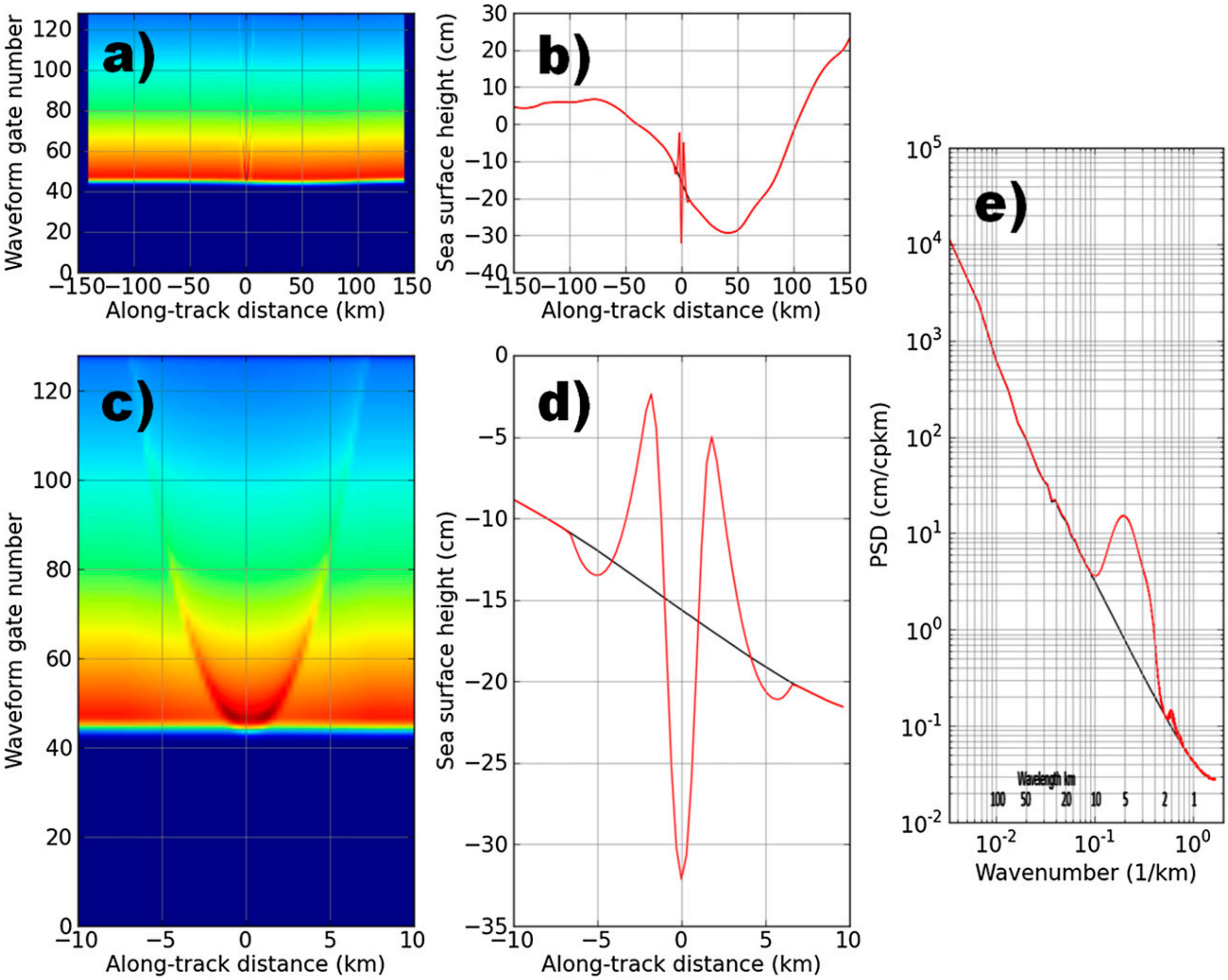

FIG. 3. Simulated response to a "sigma bloom Dirac" (300 m along track, 8 km across track, +3 dB). Waveform contamination (a) in the entire simulated segment and (c) in a 20-km zoom centered on corrupted pixels. (b),(d) Retracked SSH (red) vs the original simulated height (black), and (e) mean PSD for 25 similar 300-km samples.

Figure 3e shows the mean PSD for 25 similar samples of 300 km (simulated in black and retracked in red). The retracked SLA spectrum departs from the simulated reality from 1 to 15 km.

Although not shown in this figure, we observed that a similar anomaly and migration through the waveform is generated on the SSH if the sigma0 anomaly is negative (less power returned in a single 300-m cell). The effect of sigma0 drops is consistent with rain cell observations from Guymer et al. (1995), Quartly et al. (1996), and Tournadre (1998).

c. *Longer offset*

In the simulation from Fig. 4, we generate a 20-km-long sigma0 bloom of +3 dB; that is, the same intensity as in section 2b but on 60 consecutive Doppler bands of 300 m each. This is shorter than the length of sigma0 blooms analyzed by Mitchum et al. (2004) because in their TOPEX study, they focused only on events longer than 25 s (i.e., 150 km). In contrast, our 20-km offset is consistent with *Envisat* observations from Thibaut et al. (2007), where a large sigma0 bloom is shown to be the sum of shorter events. This offset is also consistent with the size of rain cells investigated by Quartly et al. (1996) and Tournadre (1998).

Figures 4a and 4c show that the corruption is slightly more complex: it no longer has the shape of a simple parabola, although the inner and outer edges of the transition do exhibit parabolic features.

More interestingly, waveforms and retracked parameters are *unaffected* by the +3 dB at the *center* of the 20-km bloom, that is, when the footprint measures a homogeneous +3-dB scene. This is consistent with observations from Tournadre (1998) on rain cells, in the

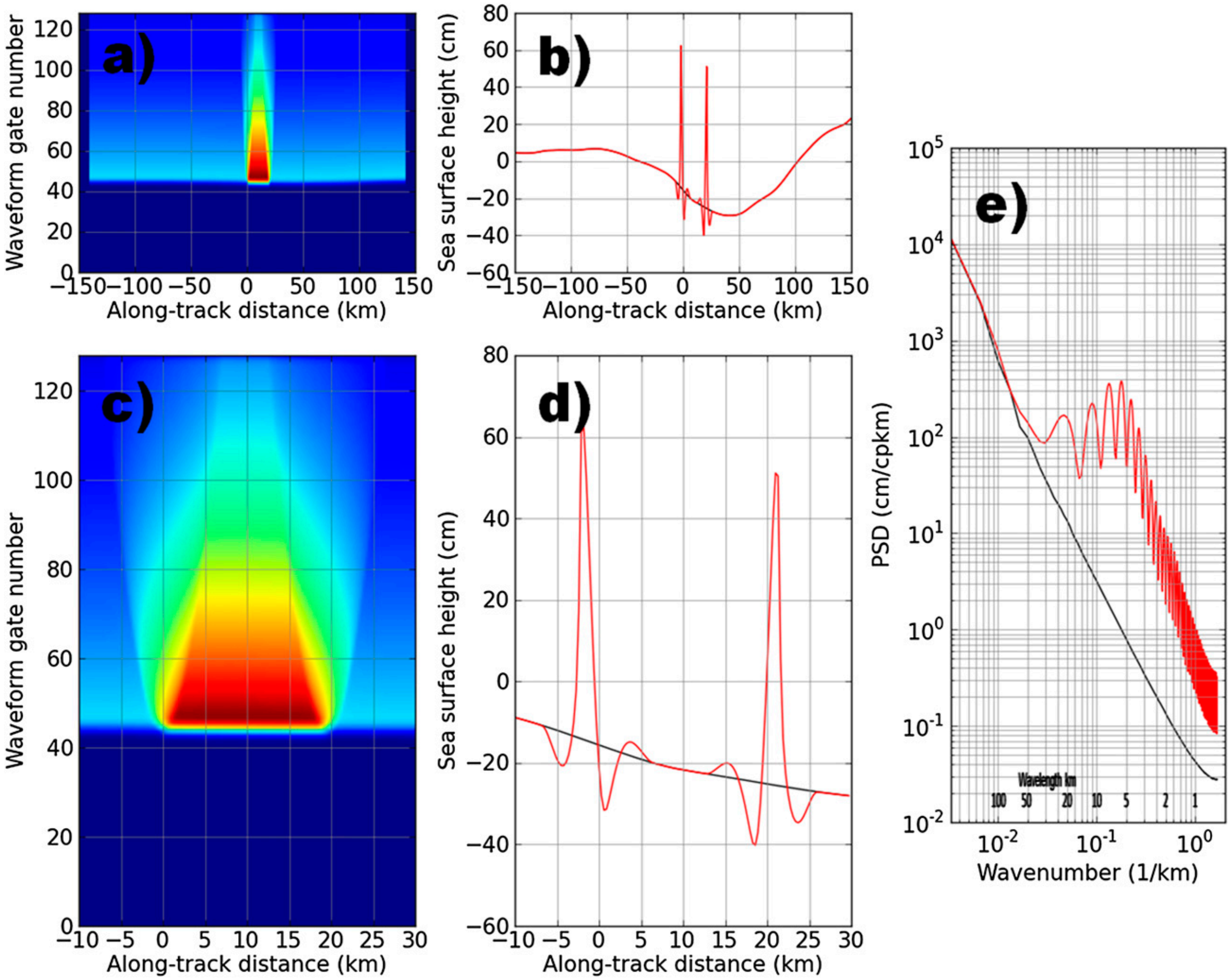

FIG. 4. Simulated response to a ''sigma bloom offset'' (20 km along track, 8 km across track, +3 dB). Waveform contamination (a) in the entire simulated segment and (c) in a 40-km zoom centered on corrupted pixels. (b),(d) Retracked sea surface height (red) vs the original simulated height (black), and (e) mean PSD for 25 similar 300-km samples.

sense that the outer edges of the perturbation (i.e., transitions and heterogeneous scenes) and the *transition* generate a stronger perturbation of the altimeter waveforms.

The right-hand-side panel of Fig. 4e shows the PSD of the simulated (black) and retracked SSH (red). For this simulation scenario, all wavelengths below 50 km are affected.

d. Other simulations and conclusions

Although not commonly studied in radar altimetry, we performed other simulations with heterogeneous SWH values in the radar footprint (e.g., SWH Dirac higher than the rest of the scene), and we obtained similar results on all retracked parameters.

The simulations give some insights on the spectral hump observed on the *Jason-2* PSD:

- The SSH error is created as soon as the LRM radar footprint captures heterogeneous values of sigma0 or SWH values because waveform retrackers cannot fit their Brown model on the corrupted waveforms. The model is insufficient to describe waveform artifacts (e.g., discussed by Quartly et al. 2001); therefore, the shape, position, and amplitude of the leading edge are corrupted beyond what was described as acceptable by Tournadre et al. (2006) for ocean slicks.
- Because of the smoothing nature of the LRM footprint, waveform artifacts are spatially coherent and so is the retracked response: even very localized backscattering events can significantly affect the spectrum of longer SLA segments, making the mean spectrum suspect up to wavelengths on the order of tens of kilometers.
- The transition between white noise floor and correlated errors happens on wavelengths ranging from the

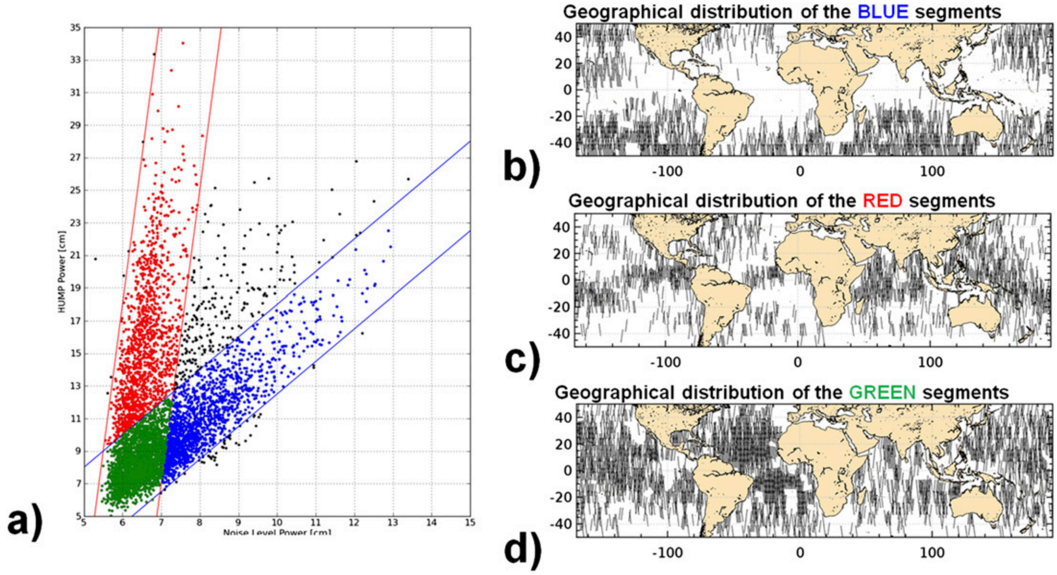

FIG. 5. (a) Scatterplot of 1000-km segments of 30 days of *Cryosat-2* data as a function of their noise energy and hump energy levels. The noise level used as abscissa is the ''white noise plateau'' (expressed in 20-Hz noise std dev) of the PSD from the 1000-km segment associated with the dot. The hump power level used in ordinate is the ''spectral hump plateau,'' observed between 10 and 20 km on the same PSD. The scatterplot is used to divide the input segments into three arbitrary populations: (b) high-waves (blue), (c) sigma0 bloom (red), and (d) standard (green). The geographical distribution of each population is given on the right-hand-side maps.

diameter of the leading edge footprint to the diameter of entire waveform footprint. This is because the retracker uses all waveform gates to fit their model, including the trailing edge and the outer circles of the footprint.

3. Analysis of actual data

In this section, we analyze actual data from multiple altimeter missions to infer how the hump artifact is modulated by instrumental parameters, the retracker used, or ancillary corrections.

a. Statistical description

To describe the statistical properties of the spectral hump, we use *Jason-2* Sensor GDR products (version D), and experimental data from *Cryosat-2* LRM processed with *Jason-2* algorithms using the level 1B product from the European Space Agency (ESA; Labroue et al. 2012; Boy et al. 2012). We use one month of data (April 2012), selecting only measurements with a latitude below 50° to avoid sea ice coverage. We consider only an uncorrected SLA—that is, the difference between the Centre National d'Etudes Spatiales (CNES) precise orbit solution and the range value from an MLE4 retracker—and we subtract the CNES/Collecte Localisation Satellite (CLS) 2011 gridded mean sea surface model.

We take *Jason-2* and *Cryosat-2* (LRM) data at 20 Hz, and we apply an editing procedure derived from Ablain et al. (2010) to reproduce a methodology commonly used by altimetry users, although this editing procedure is not designed to account for the backscatter events simulated in section 2 (the influence of the editing procedure is discussed in section 4d).

Then we split the dataset into segments [arbitrarily 1000 km, choice discussed in section 4c(1)], and we measure the 20-Hz noise standard deviation (plateau from Fig. 1) between 600 m and 1 km and the equivalent standard deviation (std dev) for wavelengths between 10 and 30 km. Note that the PSD at 30 km is *the sum* of the hump artifact and the 20-Hz white noise energy (i.e., not just the hump artifact).

Figure 5a shows the resulting scatterplot: each dot is a 1000-km segment, and the coordinates are the noise (abscissa) and hump plus noise (ordinate) energy. The scatterplot from Fig. 5 is mostly V shaped, so we arbitrarily define three populations: there is approximately 43% of low noise and low hump energy segments (green dots) in the center of the V, 27% of high noise and moderate hump energy segments (blue dots) in the right wing of the V, and 23% of high hump energy and low noise segments (red dots) in the left wing.

Higher noise levels from the blue population are mainly associated with higher SWH values, as shown by the map in Fig. 5b. Higher hump energy samples of the red population are mostly located in the tropics, the Indian Ocean, and the western Pacific (Fig. 5c), that is, in zones where the altimeter waveforms are more likely to integrate substantial inhomogeneities in backscatter strength over the footprint. Indeed, the map for the red population is quite consistent with geographical distributions observed by Quartly et al. (1996), Quartly (2010), and Tran et al. (2005) for altimeter rain flags, and by Mitchum et al. (2004) and Thibaut et al. (2010) for major sigma0 blooms (TOPEX and *Envisat*, respectively). This is coherent with the simulations from section 2: these regions are also where the retracker's model is more likely to be insufficient to describe the measured waveform, resulting in a spatially coherent error similar to Fig. 4.

The green population (low noise, small hump) can be found in all regions except at high latitudes (and to some extent in the tropics), where other populations dominate (Fig. 5d).

Figure 6 shows the mean sea level anomaly PSD for the global dataset (black curve), and for each population (colored curves). The spectral hump is clearly visible on each PSD but the hump of the red spectrum contains 3 times more energy than the white noise, whereas the green and blue spectra feature a less pronounced spectral hump (+50% from hump w.r.t the white noise energy). Note that we verified that our mean PSD are representative of the overall spectral distribution of individual spectra in each population [discussed in section 4c(1)].

These results highlight that the spectral hump phenomenon is ubiquitous on the ocean, in the sense that any long topography profile is likely to be affected, but also that a substantial fraction of the corruption of the global spectrum originates in the geographical distribution of the red population, that is, in areas where major backscattering events and rain cells are frequently observed.

However, because we use spectral analysis, we cannot determine how individual measurements are affected *within* each segment: although we display the entire 1000-km segments on these maps, it is possible—if not likely—that only a fraction of the segment is strongly corrupted like in Fig. 4. An analysis of the hump phenomenon at measurement scale (i.e., within a given segment) is discussed in sections 4d and 4e.

b. *Differences between* Cryosat-2 *and* Jason-2

The spectral humps of *Jason-2* and *Cryosat-2* (pseudo-LRM, processing described in section 4e) are different in the tropical Pacific Ocean (Fig. 1) and *Jason-2* exhibits higher spectral hump values. This raises three questions:

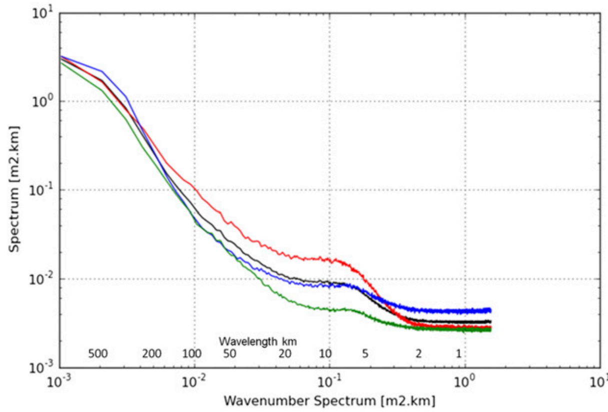

FIG. 6. Mean PSD of uncorrected *Cryosat-2* (LRM) SLA for the global dataset PSD (black) and the PSD from the three populations from Fig. 5 (colored lines).

1) Do instrumental parameters or satellite altitudes explain the differences?
2) Is the spectral hump a deterministic response to a random source (inhomogeneities in backscatter strength), as suggested by previous analyses?
3) Do data processing steps (e.g., tracker, retracker, ancillary corrections) affect this response?

Because the artifact is related to the instrument footprint, the difference between LRM and SARM (Figs. 1a and 2a) leads to SARM-specific questions. This topic is discussed in section 4e.

c. *Influence of the waveform footprint geometry*

To investigate question 1, we analyzed the differences between *Jason-2* and *Cryosat-2* (LRM). Indeed, the altitudes of both satellites are different and the instrument and antenna design are not exactly the same, resulting in a smaller waveform footprint on the latter (Fig. 2c). Furthermore, not only is the *Cryosat-2* footprint smaller but each disc/ring (i.e., pulse-limited footprint) is approximately 25%–40% smaller (disc) or thinner (annuli) than on *Jason-2* (Thibaut et al. 2012).

We projected *Jason-2* segments in the three colored distributions used for *Cryosat-2* (LRM) in Figs. 5 and 6; the *Jason-2* scatterplot and geographical distribution obtained are similar to Cryosat's (not shown) but the class distribution is slightly different: the green population contains approximately 30% of the segments instead of 43% for *Cryosat-2* LRM, and there is a wider range of noise/hump energy conditions than observed on *Cryosat-2* LRM (discussed below).

Furthermore, Fig. 7 shows the PSD of *Jason-2* and *Cryosat-2* LRM for the global ocean (left) and for the red population of Fig. 5c (right). In the top panels, the *Jason-2* SLA is derived from a standard MLE4 retracker. In the

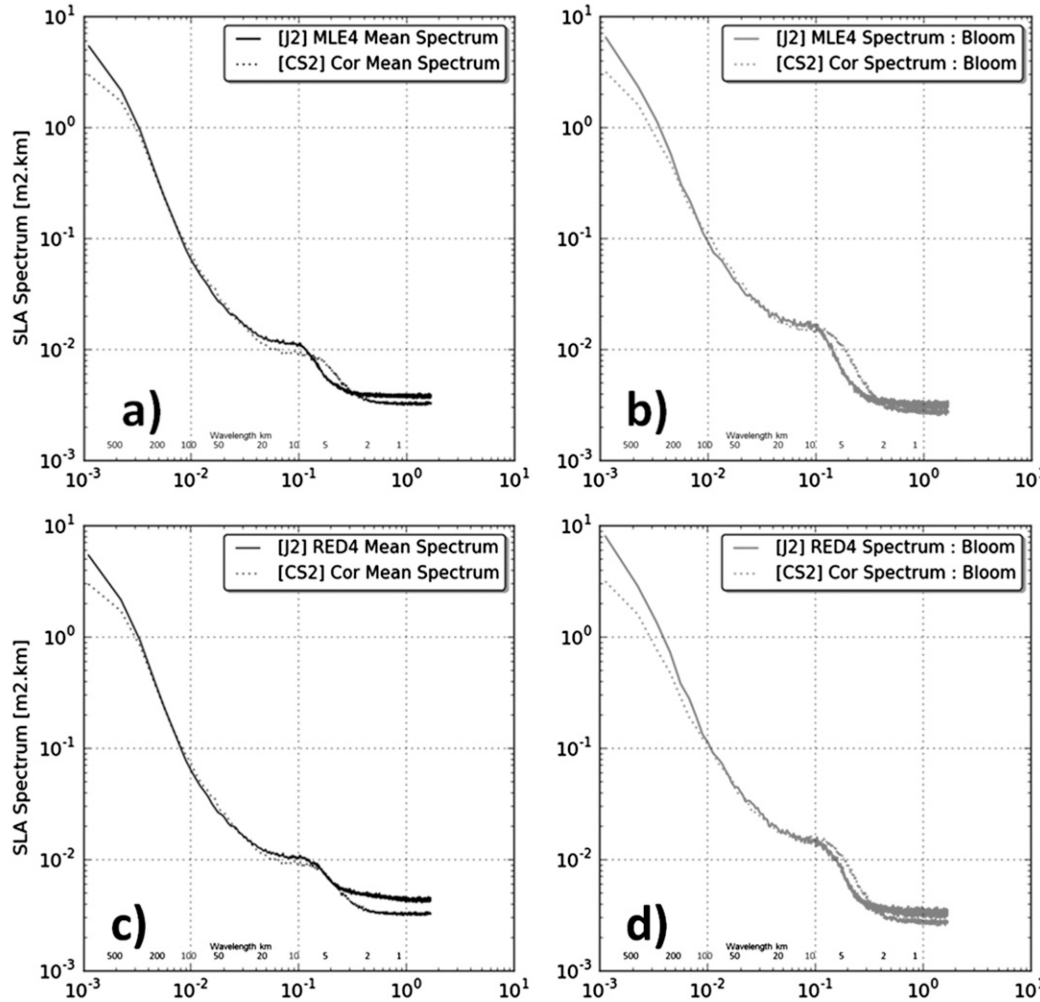

FIG. 7. (a),(b) Comparison between the mean PSD of *Jason-2* (thick solid) and *Cryosat-2* (thin dotted) uncorrected SLA (both retracked with MLE4). (c),(d) As in (a),(b), but *Jason-2* is processed with a RED4 retracker. (a),(c) Global dataset (latitudes below 50°) and (b),(d) ''sigma0 bloom population'' only.

global ocean (Fig. 7a), *Jason-2* has slightly more 20-Hz noise than *Cryosat-2*, as well as more hump energy.

More interestingly, the transition between hump and the white noise is slightly different: (3–10 km) for *Jason-2* and (2–8 km) for *Cryosat-2* LRM. The smaller value is equal to the diameter of the leading-edge footprint, and the larger value is equal to the diameter of the entire waveform footprint. This is consistent with the simulations from section 2: the error is correlated by the altimeter footprint, and it is generated even when the waveform is corrupted only in the trailing edge.

The PSD of Fig. 7b shows that in the case of the red population (highest hump values), the response of both sensors is almost the same in terms of intensity, and only the footprint-related wavelengths change. In other words, the response of both altimeters is the same when an event is picked up, and the ''mean spectral hump'' values (global spectrum, Fig. 7a) is higher on *Jason-2* because *Cryosat-2* captures *fewer* backscattering events because of its smaller footprint.

This is confirmed by the bottom panels of Fig. 7. Here, we retrack *Jason-2* waveforms with a RED4 algorithm derived from the AVISO/Coastal and Hydrology Altimetry (PISTACH) products and described by Thibaut et al. (2012). In essence, the four-parameter reduced analysis window (RED4) retracker is an MLE4 used on a truncated waveform. RED4 uses fewer waveform gates (71 as opposed to 104 with MLE4) in order to reduce the size of the waveform footprint to 8 km, that is, almost the size of the *Cryosat-2* LRM footprint. However, this method cannot change either the size of the leading edge or the size of each ring in the truncated *Jason-2* waveform.

Figure 7d shows that using a RED4 retracker on the red population slightly changes the hump response when the event is triggered: the energy of the spectral hump is slightly reduced, and the transition is slightly shifted to smaller wavelengths. Incidentally, because we use fewer waveform gates to fit the Brown model, we also increase the 20-Hz white noise.

In contrast with the red population (Fig. 7d), the global hump of the global spectra (Fig. 7c) is reduced both in intensity and in wavelengths, and *Jason-2* is much more consistent with *Cryosat-2* (albeit with the higher white noise level from RED4). The changes in the global ocean PSD are explained by the repartition of our 1000 km in the three populations: when we use the RED4 retracker, there are fewer segments in the red population and more in the green one. In other words, the statistical distribution of *Jason-2* changes to look like *Cryosat-2* LRM's. The response on intense backscattering artifacts is almost the same but the smaller waveform footprint makes RED4 capture fewer events, resulting in a cleaner global spectrum.

Altitude (and to some extent instrument and antenna design) do explain most differences between *Jason-2* and *Cryosat-2* LRM: the smaller waveform footprint, smaller leading edge footprint, thinner annuli, and better SNR provide *Cryosat-2* LRM with a lower hump response.

d. Systematic response and comparison of Jason-2 *and* Jason-1

To investigate question 2, we have analyzed data from *Jason-2* and *Jason-1* during the formation flight phase (*Jason-2* cycle 18): Fig. 8 shows the mean PSD of *Jason-2* (black) and *Jason-1* (blue), and the PSD of the difference (red) once both satellites are collocated on a common theoretical ground track. The collocation process is derived from Dorandeu et al. (2003) with a cross-track projection and an along-track re-interpolation. Both steps account for geoid gradients, as described by Dibarboure et al. (2012).

The black and blue spectra are almost perfectly superimposed, which is expected since both altimeters fly on the same ground track: the *Jason-2* and *Jason-1* tracks are in the same 1-km control band at the equator, and during the period analyzed the distance between both satellite tracks is less than 200 m.

More interestingly, the red spectrum of the difference in Fig. 8 is almost flat for all wavelengths longer than 1 km,[1] and equal to twice the white noise level (speckle related) of each Jason. In other words, the spectral humps *cancel out* in the difference: when both satellites are measuring *almost exactly* the same scene with a different speckle, the response is systematic for a given altitude, satellite design (the altimeter of *Jason-2* is almost a copy of the sensor of *Jason-1*), and processing chain, whereas the white noise is random (uncorrelated) and Gaussian.

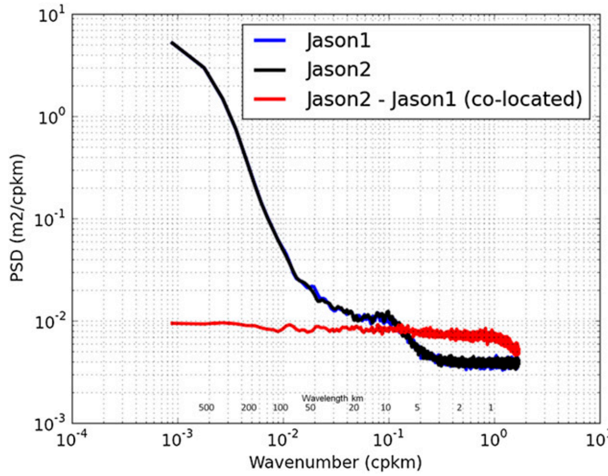

FIG. 8. Mean PSD of the uncorrected SLA from *Jason-2* (black) and *Jason-1* (blue), and the difference (red) after a collocation of *Jason-2* and *Jason-1* on a mean track. Based on 25 passes of *Jason-2* cycle 18 and *Jason-1* cycle 257.

e. Systematic response and differences between MLE3 and MLE4

To investigate question 3 and to understand the influence of the retracking method and the Brown model used, we compared *Jason-2* SSH obtained with an MLE3 retracker and the SSH from an MLE4 retracker. Amarouche et al. (2004) explain in details the differences between MLE3 and MLE4: the latter essentially estimates a fourth parameter based on the slope of the waveform trailing edge: the so-called satellite off-nadir angle (i.e., satellite mispointing). This Brown model is able to better describe how waveforms are distorted in the case of true satellite mispointing (e.g., Hayne 1980), as it was designed in response to *Jason-1* star tracker anomalies. Furthermore, Thibaut et al. (2010) reported the benefits of using MLE4 during sigma0 bloom events: MLE4 provides better retracked parameters when waveform trailing edges are affected by spurious signatures that might be mixed up with true satellite mispointing.

To illustrate, Fig. 9a shows an along-track segment of *Jason-2* waveforms during a sigma0 bloom event (left panel), and the MLE models fitted on these waveforms. The MLE3 model (middle panel) exhibits significant

[1] The energy loss for shorter wavelengths is an artifact of the collocation process, and more precisely of the along-track re-interpolation, which acts as a low-pass filter (the energy loss does not exist if we simply copy the closest value instead of using interpolation).

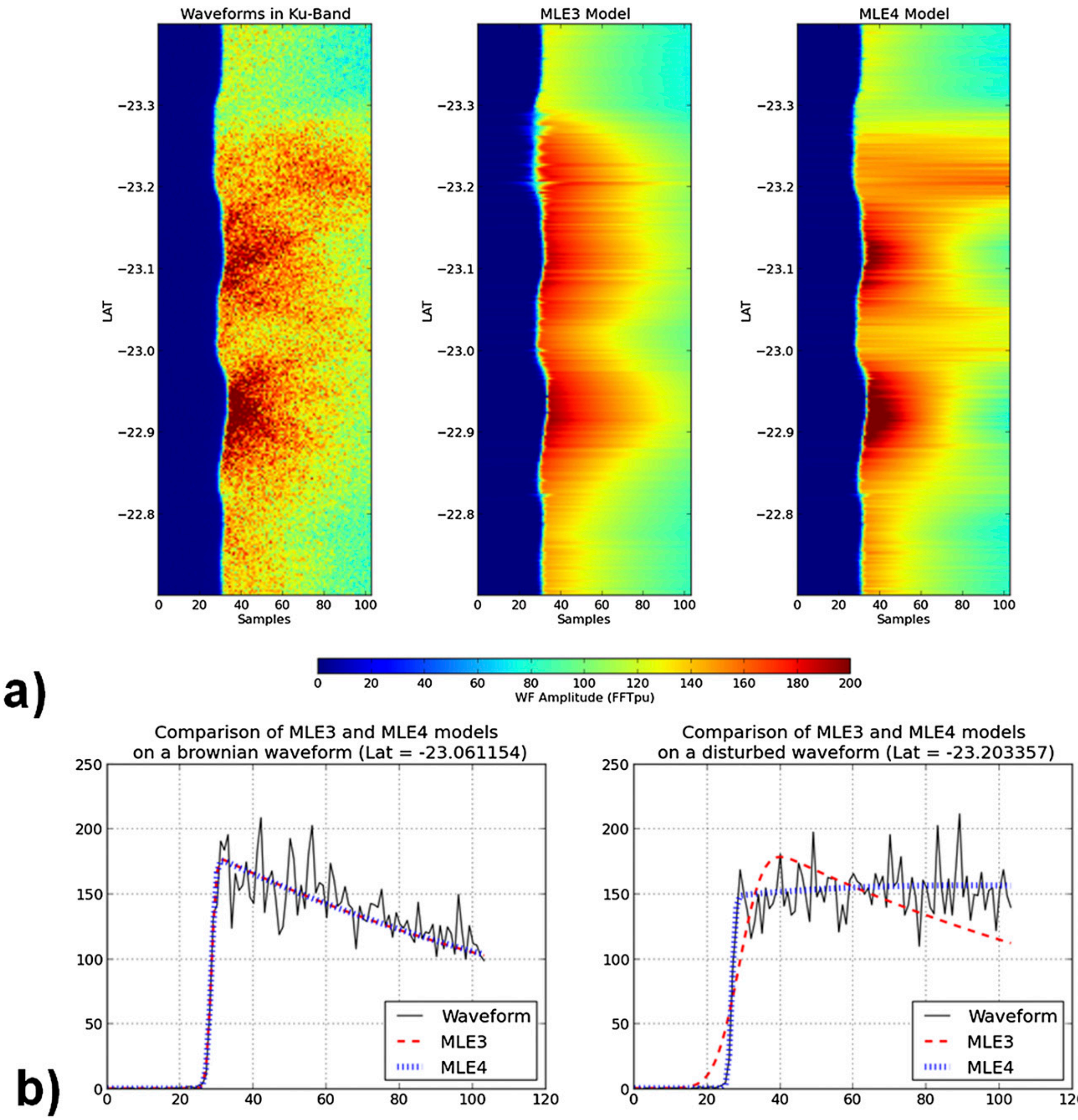

FIG. 9. (a) Along-track evolution of *Jason-2* waveforms (left) on the sigma0 bloom event described by Thibaut et al. (2010), as well as the Brownian model fitted for MLE3 (middle) and MLE4 (right). (b) Two waveform examples with the MLE3 and MLE4 fits for a standard ocean waveform (left) and for a waveform affected by the sigma0 bloom (right).

differences with the measured waveforms: the amplitude is underestimated and trailing edge artifacts are not reproduced by the MLE3 model. In contrast, the MLE4 model (right panel) is more coherent with the measured waveforms.

Figure 9b shows two waveforms in the segment from Fig. 9a: the left-hand-side plot is for a classical waveform that is barely affected by the sigma0 event. In this case, MLE3 and MLE4 are very consistent and the retracked parameters are the same. However, when the measured waveform is significantly distorted by the bloom event (Fig. 9b, right), MLE3 and MLE4 exhibit major differences. Because MLE4 estimates the slope of the trailing edge, it is able to better fit the measured waveform. In contrast, the slope of the MLE3 trailing edge is constrained and the leading edge is erroneously distorted to

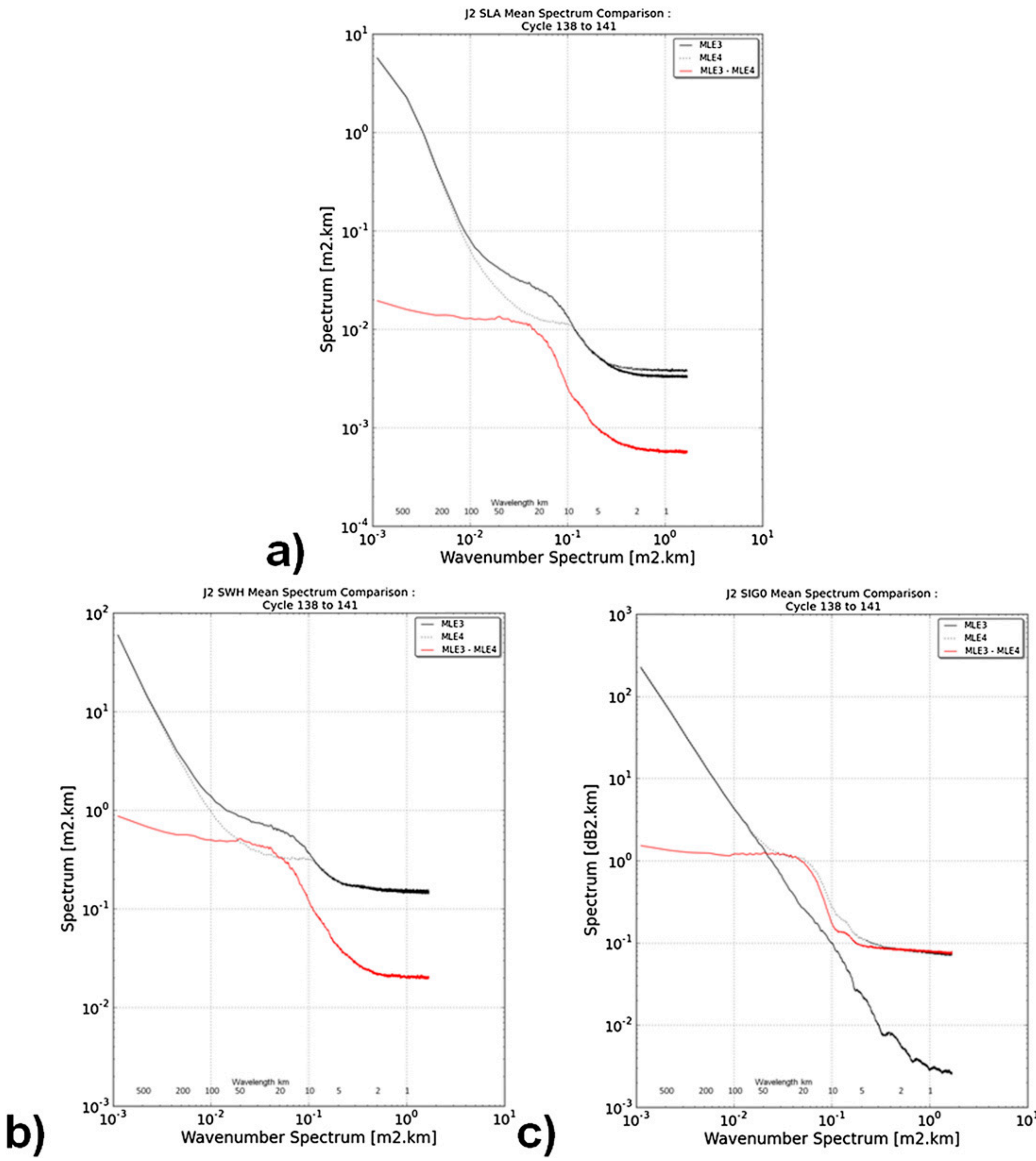

FIG. 10. Mean PSD of the *Jason-2* (a) uncorrected SLA, (b) significant wave height, and (c) sigma0 from an MLE3 retracker (black, solid) and an MLE4 retracker (black, dotted). The PSD of the difference between both datasets is shown in red.

try to minimize the differences with the measured waveform. From this simple example, we can anticipate that the waveform distortions will not have the same influence on the retracked parameters.

We performed a larger-scale comparison between MLE3 and MLE4 (from *Jason-2* SGDR, version D), and we selected our period, editing, and segment creation to ensure a perfect consistency between both PSDs.

Figure 10a shows the PSD of the SLA from MLE3 (black, solid), and the PSD of the SLA from MLE4 (black, dotted). The PSD of the difference is shown in red. Figure 10b shows similar results on the SWH power spectral density. These spectra highlight the two significant effects of adding the fourth parameter in the Brown model used by the MLE retrackers:

- The spectral hump of the MLE4 sea level anomaly is lower than the hump of MLE3 by a factor of 2, departing from the linear ocean spectrum approximately at 50–70 km instead of the 80–100 km observed with MLE3.
- The 20-Hz white noise level of SSH is slightly higher (approximately +17% on this PSD) in MLE4 because

there are more degrees of freedom when adjusting the Brown model.

Furthermore, Fig. 10c shows the results for sigma0. In this case, the MLE3 spectrum does not exhibit any hump artifact on sigma0, whereas the MLE4 does. Because the MLE3 model cannot account for trailing-edge artifacts, the corruption is primarily projected as a distortion of the leading edge, that is, on SSH and SWH, but not sigma0.

MLE4 has a different and much more moderate response to waveform corruption on SSH. This is explained by the fourth parameter and Fig. 9b: with MLE4 the slope of the trailing-edge parameter and the sigma0 estimate are absorbing the bulk of the backscattering event when the outer rings of the waveform footprint are affected. As a result, the fitted leading edge is more consistent with the actual waveform. Because the SSH and SWH parameters are derived from the leading-edge shape and position, their retrieval is more robust in MLE4.

With MLE4, the improved Brown model ''unlocks'' retracked parameters and it provides a new capability to absorb the waveform distortion as ''off-nadir angle'' and sigma0 (note that here the true pointing of *Jason-2* is very good, so the retracked off-nadir angle is only apparent). Quartly (2009a,b) also investigated the possibility of using empirical means to retrieve an ''adjusted MLE4 sigma0'' almost like in MLE3, essentially mitigating the downside of MLE4 on sigma0 and the hump observed on MLE4 sigma0.

The difference between the MLE3 SLA and the MLE4 SLA (Fig. 10a, red) also gives some insights into the systematic versus random nature of the error.

For wavelengths smaller than 2 km, the red spectra of SSH and SWH both exhibit a plateau (e.g., 5–6 $cm^2\,cpkm^{-1}$ for SSH). And the white noise plateau of the difference of MLE4 minus MLE3 is almost an order of magnitude below the white noise plateau of each MLE spectrum; that is, a large fraction of the energy *cancels out* in the MLE4 minus MLE3 difference. In other words, the noises from both retrackers are correlated (expected, since the input data, method, and model are similar), and the 20-Hz MLE4 noise is the sum of the MLE3 noise and an additional decorrelated noise stemming from the estimation of a fourth parameter.

More interestingly, the red spectra of Fig. 10 also exhibit a second plateau for long wavelengths, and a transition for wavelengths from 2–3 to 20 km, that is, the same wavelengths as the transition between MLE3 noise and MLE3 spectral hump. The second plateau is of the order of 150 $cm^2\,cpkm^{-1}$ for SSH. Furthermore, the spectrum of the difference is equal to the difference of the MLE3 and MLE4 spectra, so we can assume that 1) the MLE4 hump is *cancelled out* in the difference—that is, it is contained in the MLE3 hump; and 2) *additional* energy is observed in MLE3. In other words, the spectral hump error of MLE3 contains the MLE4 spectral hump error plus an additional MLE3-specific response to the hump origin (projected into the SSH because the apparent off-nadir angle cannot absorb trailing edge artifacts).

To summarize, the intensity of the hump artifact changes with processing choices: adding the fourth parameter and a more complex Brown model transfers the corruption of the MLE3 hump to other parameters (sigma0 and slope of the trailing edge) and smaller wavenumbers (white noise).

f. Systematic response and influence of the tracking mode

One might argue that MLE3 and MLE4 are relatively similar by design, so we also processed *Jason-2* waveforms with a simple retracker derived from *Envisat*'s ice retrackers (e.g., Laxon 1994): our so-called ICE0 retracker positions the epoch wherever the energy reaches an arbitrary value equal to the middle of the leading edge of a typical ocean waveform. While our ICE0 retracker is poorly designed in general because it barely exploits the wealth of information contained in more than 100 waveform gates, its advantage is that it is independent from the bulk of the echo and, in particular, from the trailing edge.

Figure 11 shows the average SLA PSD obtained with MLE4, with ICE0 when *Jason-2* is using the classical median tracking mode (cycles 139 and 140), and with ICE0 when the open-loop tracking mode (i.e., based on a digital elevation model) is used for cycles 5 and 7. As expected, the ICE0 retracked SLA has a high level of noise as well as undesirable energy at longer wavelengths (bias).

Yet, contrary to what is observed with an MLE4 retracker, the ICE0 algorithm exhibits two different behaviors. When the altimeter is in open-loop tracking mode (blue spectrum)—that is, tracking with an ancillary digital elevation model and not using information from previous waveform acquisitions—the spectral hump is very small and positioned on wavelengths of the order of the leading-edge footprint (as expected, since only a few gates are retracked).

However, in the more classical median tracking mode, there is a clear spectral hump. In this case, the hump comes from the median tracker itself. Indeed, the tracker computes the center of gravity of a given waveform to position the tracking window of the next acquisition. The consequence is that when the altimeter picks up

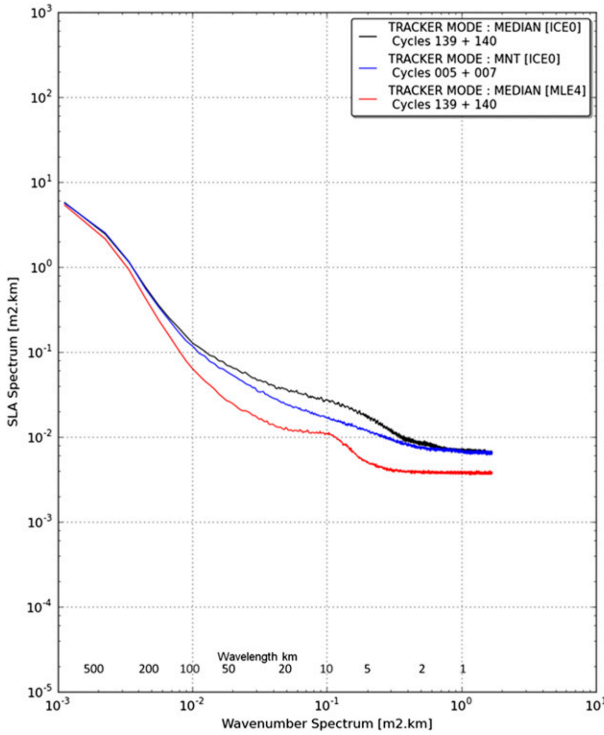

FIG. 11. Mean PSD of the *Jason-2* uncorrected SLA from an MLE4 retracker with median tracker (red), an ICE0 retracker with median tracker (black), and an ICE0 retracker with open-loop tracking (blue).

backscattering artifacts anywhere in nonzero gates, the center of gravity of the waveform is biased and the following waveform tracking is shifted. So, there is a tracker response to spurious backscattering events or rain cells (e.g., waveforms from Fig. 4) and the ICE0 retracker cannot recover the error, since it looks at a couple of waveform gates only. In contrast, the MLE4 retracker analyzes the entire waveform and it is not affected by this tracking difference. But in turn, because backscattering events or rain cells are not accounted for in the Brown model, the MLE retracker creates its own artifact.

g. *Retracker and instrument design: Other datasets and processors*

We analyzed TOPEX-derived spectra provided by the Jet Propulsion Laboratory (JPL) from both the historical product [Merged Geophysical Data Record (MGDR)] and from the retracked data [Retracked Geophysical Data Record (RGDR)] from Callahan and Oslund (2009). Figure 12a illustrates that the MGDR data derived from the onboard adaptative tracking unit (ATU; blue) exhibit low-pass-filtering features as observed by Zanife et al. (2003) and explained by the complex tracking procedure described by Chelton et al. (2001). Conversely, the RGDR spectra (black) are based on a retracker from Rodriguez et al. (2007), and they are consistent with the MLE4 spectra from both *Jason-2* and *Jason-1* (orange), up to wavelengths of the order of 5 km.[2] So, the retracking used for RGDR data (not strictly from the MLE family but also using a Brown model) is also sensitive to waveform artifacts, and the response on SSH is similar to what is observed on MLE4 on *Jason-1* and *Jason-2*.

Moreover, to understand if the two-pass retracking strategy from Sandwell and Smith (2005) was able to mitigate the spectral hump, we adapted the *Jason-1* figure from Sandwell et al. (2012), where they compare the original GDR SSH (blue) and the noise reduction obtained from their two-pass retracker (green). In Fig. 12b, we also superimpose in orange the *Jason-1*/*Jason-2* PSD from our Fig. 8. These spectra are admittedly not fully comparable, since Sandwell et al. computed their PSD on a small *Jason-1* segment (not a global dataset like in our Fig. 8). Nevertheless, Fig. 12b still shows the existence of the spectral hump both on the original GDR data and on the SSH from the two-pass retracker. The PSD estimate is noisy on this figure; therefore, it is difficult to quantify the gain in the 10–100-km band on Fig. 12b and whether the energy lost in the green spectrum is only due to white noise reduction or to a reduction of the spectral hump as well.

From these additional analyses, we can infer that the hump artifact is systematically present in LRM data from multiple missions processed with very different retrackers, although its intensity can be modulated by instrument and processing design.

h. *Influence of ancillary corrections and external parameters*

Last, we analyzed the influence of ancillary corrections and other effects: PSD computation method (direct fast Fourier transform vs least squares spectral analysis, influence of data gaps, and interpolation), MLE lookup tables, Doppler correction, wet troposphere correction (radiometer and model), dry troposphere correction, solid earth tide, pole tide, dynamic atmospheric correction, oceanic tides, dual-frequency ionosphere correction (*Jason-2*) or GPS-based ionosphere model (*Cryosat-2*), and sea-state bias (nonparametric vs parametric) as well as gridded mean sea surface [DTU10 from the Technical University of Denmark (DTU) or CLS/CNES11]. We did not observe any significant change in the spectral hump.

[2] The differences observed for wavelengths shorter than 5 km can be explained by the different strategy (waveform by waveform for *Jason-2* vs frames of 10 waveforms or 7 km for the RGDR).

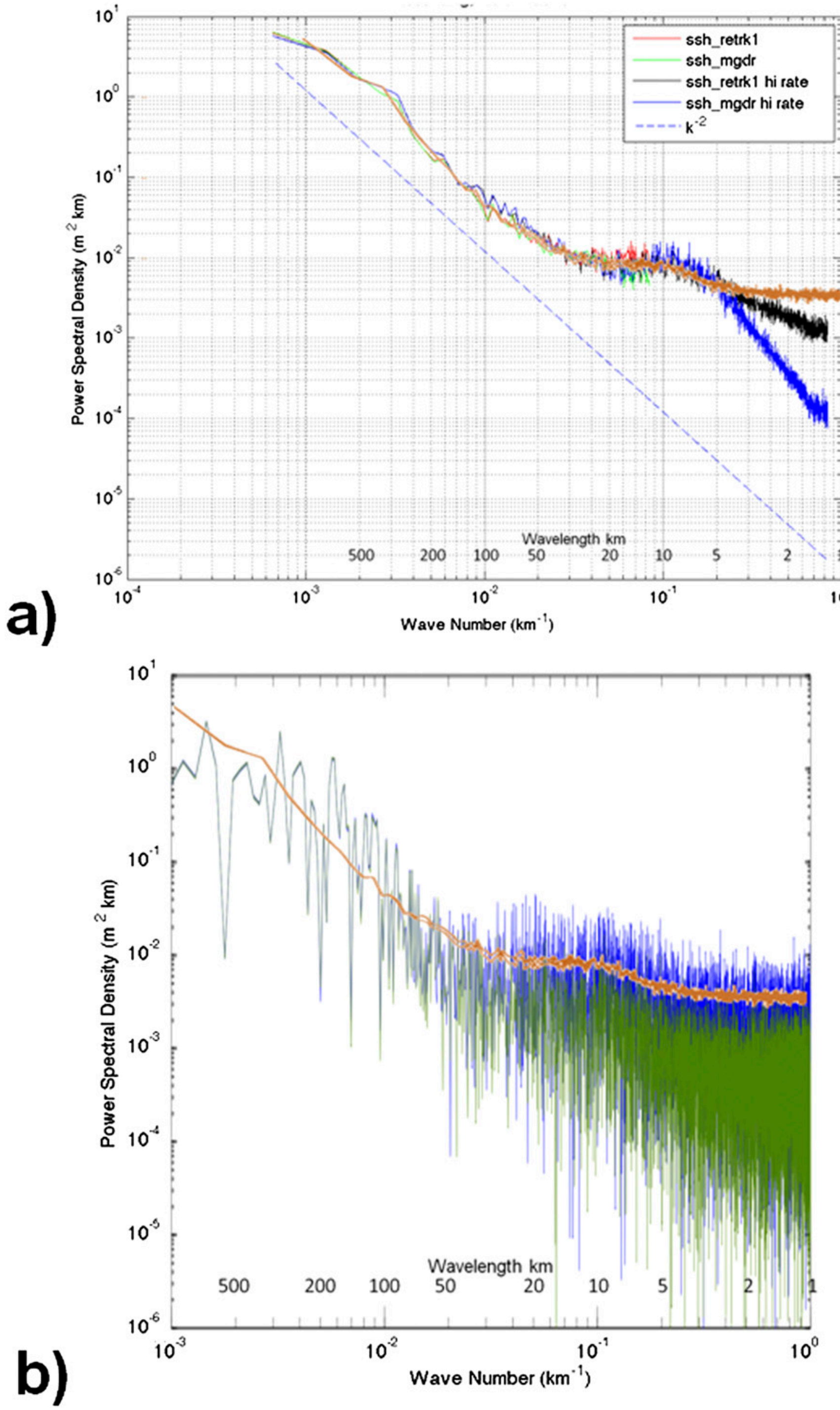

FIG. 12. (a) PSD from TOPEX SSH data, both the original onboard tracking in blue and green, and after ground retracking in red and black (P. Callahan et al. 2013, personal communication) and (b) *Jason-1* PSD from the SSH product (blue) and from SSH obtained with a double-retracking method (figure adapted from Sandwell et al. 2012). In (a),(b) we superimpose the *Jason-1* and *Jason-2* SSH PSD from Fig. 8 (orange curves).

i. Outlook

Our findings indicate that space agencies and instrument processing experts might be able to develop new processing algorithms to better detect or mitigate the LRM artifact. There are many methodologies that could be adapted and tested to better handle the LRM hump: better Brown models for MLE-class retrackers, or other Brown-derived retrackers with fewer approximations [e.g., derived from the numerical forward modeling approach from Phalippou et al. (2007); Phalippou and Demeestere 2011], or dedicated waveform analyzers [e.g., 2D maps of backscatter inhomogeneities from Quartly (1998)]; matching pursuit algorithm (Tournadre et al. 2009), or LRM waveform cleaning [e.g., singular value decomposition described by Ollivier (2006) or Thibaut et al. (2012); hyperbolic pretracker from Quartly (2011); or two-pass approach from Sandwell and Smith (2005)].

4. Discussion

a. Link with the ''noise'' level observed on 1-Hz data

Figure 1 and section 3 expanded on the statements from Faugère et al. (2006): the plateau observed on 1-Hz spectra might be misleading, since it is not truly a Gaussian noise, but an ''apparent noise'' merging instrumental noise and spectral hump energy. In that context, an important observation is that instrumental noise increases with SWH (e.g., Zanife et al. 2003), whereas the spectral hump does not.

With the blue population of our Fig. 5a, we specifically target segments with a *moderate* hump energy and large instrumental noise: we focus on the effect of waves, but we exclude backscattering events or rain cells, so we rule out a significant amount of segments with high noise *and* high hump levels.

In contrast, the black dots from Fig. 5a give a fourth population with both high 20-Hz noise *and* spectral hump. This population is located in the same zones as the blue population and it has a spectral hump similar to the red population (not shown). The presence of the hump at high latitudes is consistent with observations from Quartly et al. (1996), Quartly (2010), and Tran et al. (2005) because the rain flag of Jason detects many spurious backscattering scenes at these latitudes as well.

Finally, if we merge the blue and black populations from Fig. 5a, we obtain the relationship between the 1-Hz apparent noise and SWH (e.g., Faugère et al. 2006). This classical relationship is, however, hiding that two effects are combined and only one is SWH dependent.

b. Influence of 20–1-Hz processing

In section 3d we observed that the spectral hump of *Jason-2* and *Jason-1* are correlated; that is, they cancel out in the *Jason-2* minus *Jason-1* difference during the tandem phase. But this observation on 20-Hz rate measurements cannot be reproduced with 1-Hz data, even though the latter are a low-resolution dataset derived from the former.

We consistently find (not shown) that the 1-Hz *Jason-2* minus *Jason-1* difference exhibits a flat spectrum with significantly more energy than the 20-Hz difference. At 1 Hz the apparent noise for wavelengths ranging from 15 to 30 km has the correct amount of energy (same level as the 20-Hz hump) but it no longer cancels out in the difference. The coherency between *Jason-2* and *Jason-1* artifacts disappears from 20 to 1 Hz: oceanography users can use 1-Hz data only as long as they do not investigate the correlation between both missions for high wavenumbers.

To investigate the influence of 1-Hz processing, we have reproduced this effect (with the simple simulations from Fig. 15a). We created 1000 simulated SSH segments for *Jason-1* and *Jason-2* (perfectly collocated at 20 Hz). We used two independent white noises (one for each satellite, no correlation), which we added to common SSH and spectral hump simulations (same values for both satellites). Then we computed the average PSD of each sensor and the difference (black spectra from Fig. 16a). By construction, the difference between our simulated 20-Hz *Jason-2* and 20-Hz *Jason-1* is flat and with the energy of both independent noises. This is consistent with Fig. 8. At 20 Hz, the SSH and hump are cancelled out by the difference, whereas white noises add up.

Then we used idealized processing to downgrade each dataset to 1 Hz; that is, we created our 1-Hz samples with the standard packet averaging used in the Jason ground segments but we ensured a perfect coherency between the limits of the packets of 20 measurements for *Jason-1* and *Jason-2* and we applied no editing whatsoever. The resulting 1-Hz spectrum is perfectly consistent with what is observed at 20 Hz (black spectra, right panel in Fig. 13). This is what 1-Hz altimetry users would intuitively expect from the findings of section 3d.

However, when our simulated packets of 20 measurements are not spatially coherent (e.g., when the *Jason-2* packets start/end in the middle of the *Jason-1* packets) and when we artificially edit out a small amount of isolated measurements (reconstructed with linear interpolation), we are getting a 1-Hz difference with more energy than the expected 20-Hz reference (green

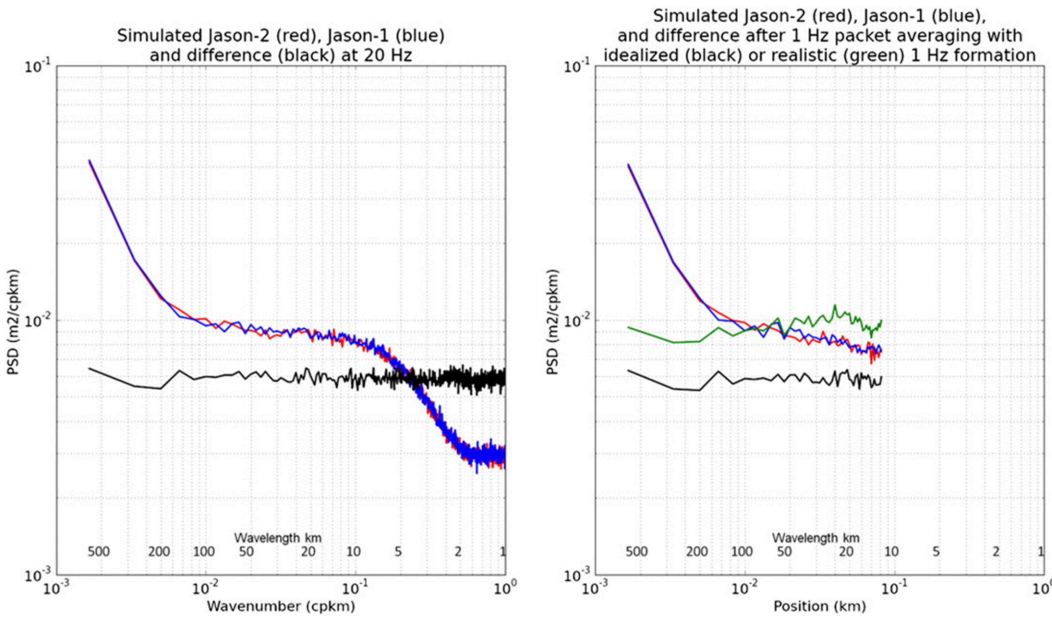

FIG. 13. Simulation of the different behavior of *Jason-2* minus *Jason-1* differences at (left) 20 and (right) 1 Hz. When the SSH and the spectral hump are coherent for *Jason-2* and *Jason-1* but not for the instrumental white noise, the 20-Hz differences (left, black) are consistent observations from Fig. 8. The (right) is for 1-Hz data when *Jason-2* and *Jason-1* packets are spatially coherent and with no 1-Hz editing (black), and for ''interleaved packets'' between *Jason-2* and *Jason-1* and after 1-Hz editing (green).

spectrum in Fig. 13). This is what 1-Hz altimetry users can observe on actual products.

The only difference between the ''good' (Fig. 13, black) 1-Hz spectrum and the ''bad'' (Fig. 13, green) one is how we selected our 20 measurements to create the 1-Hz packets, and how we created/filled small gaps with 1-Hz editing on each Jason satellite. The compression from 20 to 1 Hz and the 1-Hz editing and gaps induced a significant loss of coherency between our 1-Hz-simulated *Jason-2* and *Jason-1* samples, which were—by construction—perfectly coherent at 20 Hz.

To reproduce this effect on actual data is complex because one would need to perform a concurrent reprocessing of the GDR record of both *Jason-2* and *Jason-1* during the tandem phase: to create custom 1-Hz data from the original 20-Hz samples and more specifically to ensure a good coherency between the packets and editing (something not done in the GDR processors).

c. *How random is the spectral hump artifact?*

The simulations from section 2 and the analyses from section 3 give some insights about the origin of the error and about the modulation by instrumental parameters or processing algorithms. But two questions were not discussed so far:

1) Is there a continuum of ''hump intensity'' or is the spectral hump limited to small subsets of data? In other words, is the probability density function of the hump artifact continuous or the result of a marginal outlier population (e.g., red population from section 3a)?
2) Is the spectral hump limited to some wavelengths (e.g., dome-shaped spectrum like in Fig. 3e), or a red-colored noise (i.e., energy decreasing with wavenumber k), or a random Gaussian signal (i.e., flat spectrum).

1) CONTINUUM OF SPECTRAL HUMP CORRUPTION

To investigate the first point, we took the blue spectrum from Fig. 1a, that is, the PSD based on *Cryosat-2* pseudo-LRM (see section 4e). Figure 14a shows the mean spectrum (thick white line) based on the averaging of 2000 individual spectra, and the colored background shows the distribution of the individual spectra in wavelength/power density bins. There is clearly a single population, and the mean spectrum is at the center of the distribution of individual spectra (i.e., dark red/black envelope). The mean spectrum is not altered by a small population of outliers.

Furthermore, the thin white lines of Fig. 14a show the 10%–80% percentiles of the distribution of individual spectra for each frequency. The spectral hump is consistently visible on all white curves; that is, the artifact

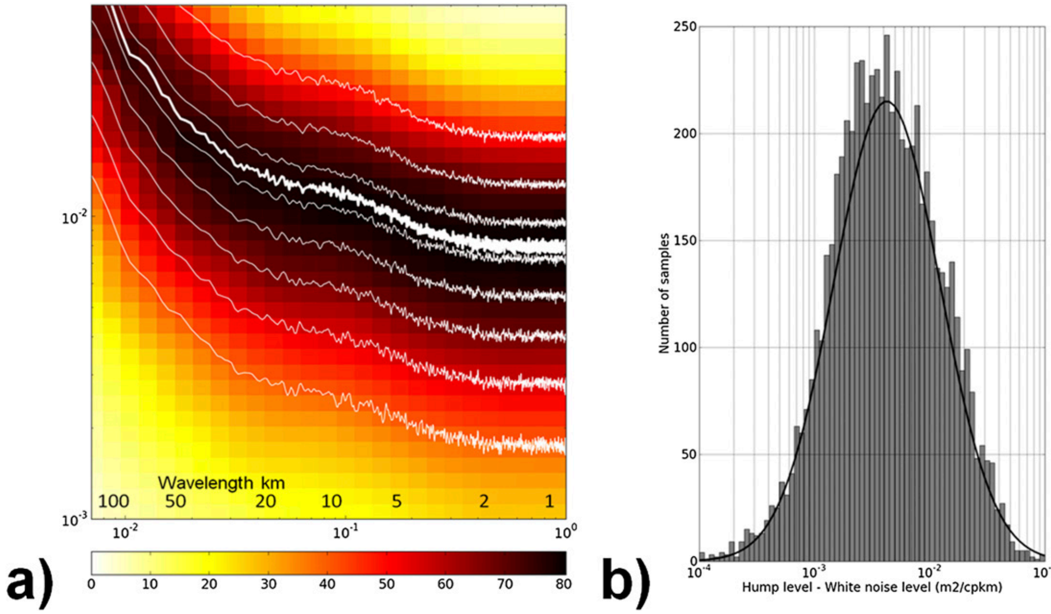

FIG. 14. (a) Thick white line shows the mean PSD of the *Cryosat-2* PLRM dataset (i.e., the blue spectrum from Fig. 1a) superimposed on the distribution of individual spectra used in the averaging: the colored background shows the number of samples in wavelength/power density bins out of 2000 individual spectra. Thin white lines show the 10%–80% percentiles of the distribution for each frequency. Units: wavenumber in cpkm (abscissa) and power density in $m^2\,cpkm^{-1}$ (ordinate). (b) Logarithmic scale shows the global distribution of the *Jason-2* hump energy from Fig. 8 with a fitted Gaussian model.

exists even on the 10% isopercentile: it is very difficult to get hump-free data unless a large majority of the altimeter segments is sacrificed. The energy associated with the hump of isopercentile lines increases continuously: there is a continuously decreasing probability to encounter strong humps in our 1000-km segments. For the 10% isopercentile, the hump barely has enough energy to go above the noise floor, and it is possible that in a different configuration (mission, zone, period) the hump would be below the noise floor, that is, not visible on individual spectra or the 10%–30% percentile.

To better characterize the corruption continuum, we also used the *Jason-2* scatterplots from section 3a, where each segment is displayed in the noise (abscissa) and hump plus noise (ordinate) plane. We then compute the difference between the energy at 10–30 km and the energy 0.6–1 km to obtain, for each segment, the average energy of the hump *only*. Figure 14b shows the distribution of this *Jason-2* hump energy on a logarithmic scale. The distribution is clearly continuous with a single bell-shaped population: the hump is not the result of a marginal subset of segments.

This finding underlines that major backscattering artifacts, such as rain cells or sigma0 blooms (e.g., red population from section 3a), might be only the most visible artifacts of a more widespread random phenomenon of smaller amplitude. Because of the random nature of the phenomenon, a large majority of long SSH segments are affected.

Note that the spectral analysis does not analyze the distribution within each individual segment, so we cannot yet determine how continuous the probability is of finding erroneous individual measurements within each segment. Sections 4d and 4e provide additional insights on this question.

2) WHITE COLORATION OF THE SPECTRAL HUMP

To illustrate the possible spectral coloration of the hump error, Fig. 15a shows a simple proxy of the mean MLE4 PSD from Fig. 10a: we created an idealized SSH spectrum (dotted line) as the sum of a k^{-2} law and white instrumental noise. Then we added a flat Gaussian spectrum (dashed line) correlated by the altimeter footprint (i.e., low-pass filtered with a half-power cutoff of 10 km) and we obtained the proxy (solid line, thick). In contrast, the proxy from Fig. 15b is created with a similar process, but this time assuming the spectral artifact is dome-shaped like in the simulations from section 2.

Although both proxies (solid line) exhibit a spectral hump, the PSD of the artifact itself (dashed line) is very different. Moreover, it is somewhat difficult to determine the exact shape of the hump from the total PSD because the SSH and/or white noise (dotted lines) have

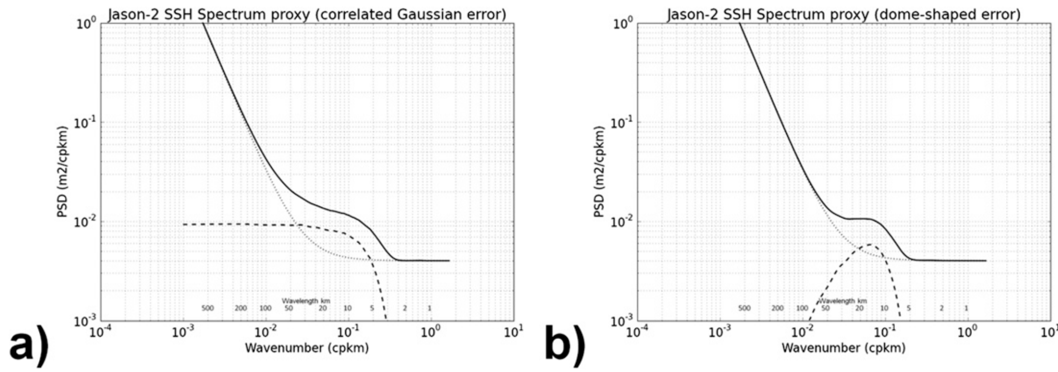

FIG. 15. (a),(b) Simulation of the black spectrum from Fig. 8 (solid line), where (a) is assuming that the "spectral hump" (dashed) is a random Gaussian process with a 10-km correlation (half-power cutoff) added to the conventional "signal plus white noise" assumption (dotted), and (b) is for a dome-shaped hump spectrum.

more energy than the correlated error (dashed lines). Similarly, it is somewhat difficult to determine whether the spectral hump is Gaussian based on actual SSH spectra computed using long segments.

This question is relevant in the context of oceanography studies focusing on the slope of the SSH spectrum (e.g., Richman et al. 2012; Sasaki and Klein 2012; Scott and Wang 2005) because the spectral hump is artificially corrupting the SSH slope to artificial lower values up to 70 km or more.

To get a robust spectral slope estimate, Le Traon et al. (2008) focused on wavelengths larger than 100 km, where the spectrum is supposedly not affected by the error thanks to a more favorable signal-to-noise ratio. In contrast, Xu and Fu (2012) estimated their spectral slope on wavelengths as small as 70 km, and they removed a constant value estimated from 15 to 30 km for each spectrum. Their approach allows them to unbias the slope value from the PSD curvature due to the 1-Hz white noise (spectral plateau). With this method, the underlying assumption is that the error observed from 15 to 30 km is a random Gaussian process with a flat spectrum; that is, the value of the 1-Hz plateau can be used as a constant correction for longer wavelengths.

Our Fig. 1a shows that the error observed between 15 and 30 km is not the instrumental Gaussian white noise, as the latter is visible only on 20-Hz spectra. Instead, Xu and Fu correct their spectral slope from the spectral hump. Consequently, their method is valid only if the spectral hump has a flat spectrum (e.g., proxy from Fig. 15a). Yet, the approach is not valid if the spectral hump is dome shaped or red-colored noise (e.g., proxy from Fig. 15b) because the value estimated at 15–30 km cannot be used for other wavenumbers.

In our simulations, we showed that local backscattering events (Figs. 3 and 4) generated dome-shaped spectral corruptions, not correlated Gaussian noise. This can be explained by the nature of our simulations, where the sigma0 event is simulated in cells of 300 m along track and 7 km across track. Indeed, because the corrupted cell always crosses the nadir track, the resulting waveform artifacts (parabolic migration) have a dominant scale, that is, a dome-shaped PSD. Yet, smaller zones can generate corruptions only on the outer rings of the footprint, that is, only the waveform trailing edges. In this case, a wider range of signatures would be observed on the retracked parameters.

To further investigate the smoothed but Gaussian nature of the spectral hump on long segments, we used the MLE4 spectra from Fig. 10a, and we subtracted an idealized PSD (like in Fig. 15) that is created as the sum of a linear fit on the SSH and noise (Fig. 16a, dashed lines). The residual hump PSD (Fig. 16a, red) exhibits a very flat plateau of the order of $7 \times 10^{-3}\,\mathrm{m^2\,cpkm^{-1}}$ from 10 to 50 km. In Fig. 16b, we performed the same analysis for the spectra from Fig. 6 and we find a consistently flat plateau for the global ocean, the green and red populations (moderate and energetic spectral hump, respectively). Figure 14b also shows that the statistical distribution of the hump artifact intensity is well approximated by a flat spectrum. In other words, if a large amount of long segments is used, then one can assume that the spectral hump has a flat spectrum.

Not only does this result justify the method used by Xu and Fu (2012) but also explains why the spectral hump artifact is difficult to detect in general: it can be misinterpreted as instrumental noise by oceanographers who use long segments of 1-Hz data. It also explains why the studies that do use the 20-Hz rate (e.g., Birol et al. 2010; Bouffard et al. 2010; Dussurget et al. 2011) can reduce the spectral hump error when computing temporal averages or when using noise reduction processing that is statistically valid only for random errors.

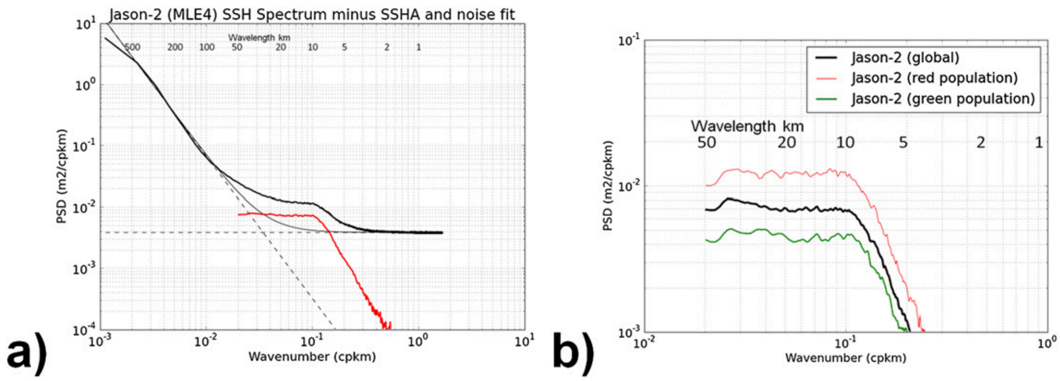

FIG. 16. (a) Estimation of the *Jason-2* hump spectrum (red curve) computed as the residual between the MLE4 *Jason-2* spectrum from Fig. 10 (black curve, solid, thick) and the idealized SSHA spectrum (black curve, solid, thin). The idealized SSH spectrum is the sum of a linear adjustment of the true SSH spectrum from 70 to 300 km and a noise constant estimated on the SSH spectrum from 600 m to 2 km (black curves, dashed). (b) Hump residual [method from (a)] applied to the *Jason-2* population from Fig. 5.

d. Mitigating the hump artifact with better 20-Hz editing procedures

We have shown that the signal originating the LRM spectral hump is in the altimeter waveforms themselves, that is, in raw data collected by LRM altimeters. The signal is turned into an SSH error by current waveform retrackers because they are not designed to handle this signal. Furthermore, its random nature makes it difficult to detect and to reduce the error on 1-Hz data.

This finding raises a practical question from the altimetry user's point of view: can we postprocess the long series of LRM records and mitigate the corruption of the retracked parameters? In other words, can we use the 20-Hz rate of existing GDR products to recover a fraction of the oceanic variability that might be locally hidden by the spectral hump corruption? To investigate this, we compared three simple editing procedures on one month of *Cryosat-2* LRM (Fig. 17a):

(i) The black spectrum is based on the 1-Hz editing flag derived from Ablain et al. (2010) and duplicated on the 20 high-rate measurements. This editing was designed for calibration/validation purposes, and it is not optimal for detecting and removing rain or backscatter events, that is, to mitigate the hump artifact.

(ii) In contrast, the blue spectrum is based on the same raw data, but it is based on a different editing scheme: we inject all SSH data at 20 Hz into an nonlinear iterative editing filter that iteratively removes individual SLA values that depart from low-pass-filtered SLA (cutoff: 50 km) beyond 3-sigma of the local standard deviation. This filter was used by Labroue et al. (2012) and is applied operationally in the AVISO processing chain described by Dibarboure et al. (2011).

(iii) Similarly, the red spectrum uses a simple 20-Hz strategy derived from the rain detection procedures of Tournadre et al. (2009). We compute the standard deviation of the along-track SLA in a small running window (e.g., 15 km), and we edit out all measurements in a given window if the standard deviation goes beyond a given threshold (e.g., 10–20 cm).

There are two major differences between the editing scheme of Ablain et al. (2010) and the other procedures: 1) the former is used at 1 Hz, whereas the others exploit the small-scale content at the 20-Hz rate; and 2) the 20-Hz algorithms focus on detecting unusual small-scale dynamics; thus, they are more prone to detect intense and local backscatter events like those simulated in section 2.

In Fig. 17a, we chose threshold parameters that remove approximately the same number of measurements: 2.4%–2.7% of the input data. Yet, although the same number of measurement is kept, Fig. 17a exhibits a substantial (30%) mitigation of the hump when the 20-Hz rate editing is used. The hump phenomenon is still continuous when globally observed on long segments [section 4c(1); Fig. 14b], but the continuum has been shifted to lower values (i.e., closer to the white noise floor).

We also used more aggressive editing parameters to further mitigate the hump artifact. As expected, this comes with a toll on coverage: when the running standard deviation editing scheme is used (red spectrum in Fig. 17a), it is possible reduce the mean hump energy by a factor of 2, yet the number of edited measurements

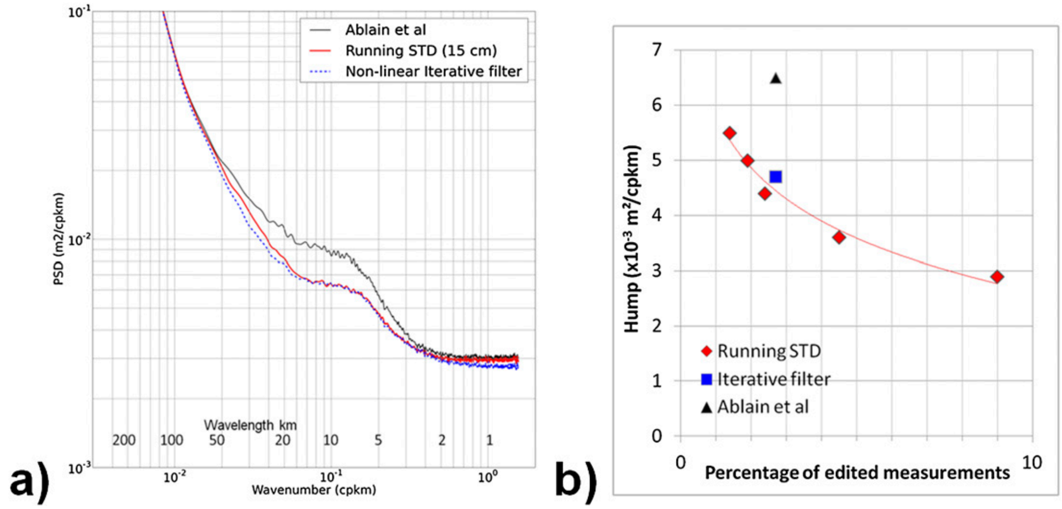

FIG. 17. (a) Mean PSD of one month of uncorrected *Cryosat-2* SLA with three editing processes: 1-Hz editing from Ablain et al. (2010; black), 20-Hz running standard deviation threshold (red), and 20-Hz nonlinear iterative editing filter (blue). (b) Mean hump energy (spectral level at 15 km minus white noise floor level) as a function of the percentage of edited measurements for three editing processes and parameters.

increases from 1.5% to 9% (Fig. 17b). The red logarithmic fit in Fig. 17b shows that to remove the hump artifact entirely (i.e., to make it disappear below the white noise floor), it is likely necessary to edit out a substantial amount of 20-Hz measurements. Figure 17b still shows that it is possible to design much more efficient editing schemes than the classical 1-Hz procedures.

Oceanographers with an interest in small-scale content should *always* use the 20-Hz record and develop sophisticated editing, filtering, or postprocessing schemes 1) to mitigate the spectral hump and 2) to keep a good coverage of altimeter measurements.

e. *Observations from SARM altimetry and implications for future missions*

1) BENEFITS OF A SARM ALTIMETER FOR SHORT-WAVELENGTH TOPOGRAPHY

Preliminary findings from Boy et al. (2012) highlighted that the spectral hump was not visible in the PSD derived from *Cryosat-2* SARM: Fig. 1a shows the 20-Hz PSD derived from *Jason-2* in black (GDR product) and *Cryosat-2* SARM in red; both datasets are from May to June 2012 and from the *Cryosat-2* SARM acquisition zone of the tropical Pacific Ocean (green box in Fig. 1b).

The SARM-retracked SSH is generated by the processing prototype from CNES (Boy et al. 2012). The blue spectrum from Fig. 1a is the PSD of so-called pseudo-LRM data (or PLRM), that is, LRM-class generated from raw SARM data. PLRM is generated by the same prototype following a methodology described by Martin-Puig et al. (2008), Boy et al. (2011), and Amarouche et al. (2013a). Despite the higher noise floor level associated with PLRM processing, the hump is visible when SARM is downgraded to LRM class.

More importantly, the SARM spectrum (Fig. 1a, red) exhibits two notable features:

1) The smaller SARM footprint (Fig. 2) eliminates the along-track smoothing observed on LRM altimetry data.
2) SARM white noise is almost (but not entirely) explained by instrumental parameters.

Feature 1 is the most important because—in theory—SARM altimetry not only reduces the white noise level [more pulses averaged in one echo, as per Phalippou et al. (2001)] but also provides better observations of small mesoscale because the LRM spectral hump does not exist in SARM altimetry. At 10 km, the error level observed on *Jason-2* is approximately 5 times higher than for *Cryosat-2* SARM. This is admittedly an upper estimate because the SARM acquisition zone of Fig. 1 is also where the red population from Fig. 5 dominates.

In the 10–100-km band, the red spectrum is also more realistic: in SARM, the linear trend of the PSD is almost valid down to 50 km, and scales as small as 30 km should not be contaminated by more than 50% error as opposed to the 70–80 km of LRM. Furthermore, if we apply geophysical corrections to the data from Fig. 1, the spectral slope observed from 70 to 200 km on *Jason-2* (LRM) SLA in the area from Fig. 1 is approximately

k^{-1}, that is, agreeing with values by Xu and Fu (2012) in this region when their bias correction is not applied. Their revised value after a spectral correction of the LRM noise is $k^{-1.4}$. In comparison, the *raw*, *unaltered*, spectral slope of SARM data is $k^{-1.2}$. Not only is the SARM spectrum cleaner because of smaller errors from 10 to 100 km but the spectral slope is also more consistent with their *corrected* values from LRM. Residual differences might even be explained by actual oceanographic content from internal tides (Richman et al. 2012) that are hidden by LRM noise. Indeed, the western part of the tropical Pacific Ocean SARM acquisition zone from Fig. 1 is located where internal tides have a high amplitude (e.g., Richman et al. 2012) and where mesoscale variability is low (e.g., Dibarboure et al. 2012) and below the noise level of *Jason-2*.

Therefore, the value of SARM lies not just in the observation of 1–10-km features (e.g., coastal fronts, geodetic/bathymetric topography signatures) from reduced white noise but also in the ability to create a more trustworthy dataset of SLA to observe scales ranging from 10 to 100 km. The benefits would range from direct ocean observation (e.g., large submesoscale, internal tides, infragravity waves) to regional and global model assimilation and better monitoring of small-scale dynamics for long-term climate records.

Furthermore, feature 2 is also important. In the simulations from section 2, the SARM retracked parameters do not exhibit any corruption. This is explained by the ''ideal'' simulations we perform: we create a sigma0 bloom in the *entire* SARM synthetic footprint. So, the SARM waveform is not affected by the heterogeneity affecting LRM. But it is possible that using a more sophisticated simulator, such as ESA's Sentinel-3 Performance Simulator (SPS; Amarouche et al. 2013b), one could analyze scenes where only *half* the SARM footprint is on a sigma0 bloom. To that extent, future investigations might find that SARM also responds to heterogeneous backscattered scenes, generating an additional Gaussian-like noise [see section 4c(2)] without the along-track LRM smoothing.

Yet, Fig. 1 illustrates that there is little white noise that cannot be explained by the instrumental parameters of *Cryosat-2*'s altimeter. In other words, if a Gaussian-like noise does exist in SARM, then the retracker from Boy et al. (2012) exhibits a weak response to backscatter inhomogeneities in the footprint, and especially in the tropical zone where LRM data exhibit a very high spectral hump signature. This is possibly because SARM waveforms are peakier (stripe-shaped geometry of the synthetic footprint) and because corruptions in SARM waveforms affect other retracked parameters but not the epoch.

2) Concurrent use of PLRM and SARM to detect hump events

An asset of *Cryosat-2*'s delay Doppler is to provide concurrently SARM and PLRM measurements. Although the white noise level of the PLRM measurement is higher than its LRM counterpart, the dual measurement makes it possible to confirm the assumptions from section 2: SARM *does* observe rapid changes in backscatter strength that are smoothed in PLRM.

This phenomenon is visible in Fig. 18a along a 400-km segment of *Cryosat-2* track. The PLRM sigma0 (red) and SARM sigma0 (blue) are very consistent on scales larger than the LRM footprint even though the retracker used for SARM and PLRM are very different. However, there are many occurrences of peaks in SARM sigma0 that range from less than 1 to 10 km. In contrast, the PLRM sigma0 is generally smoother. On this segment, the differences between the PLRM and SARM sigma0 range from 0.1 to 1 dB (i.e., much less than the 3 dB of the simulation of Fig. 3).

To verify that these peaks were true signatures from hump-generation events and not just artifacts from the SARM retracker of Boy et al. (2012), we used the differences between SARM and PLRM sigma0 as a criterion to edit PLRM measurements. To minimize false detections, we also applied a low-pass filter on the sigma0 differences to edit only spatially coherent events. The edited segments are highlighted with gray boxes in Fig. 18a.

Figure 18b shows that using the differences between SARM and PLRM sigma0 as an editing criterion has a positive effect on the PLRM hump artifact: the blue spectrum exhibits very little corruption, whereas the red PSD did contain a clearly visible hump. Note that the red spectrum was generated with the same PLRM dataset and with the nonlinear iterative editing filter from section 4d (i.e., the hump of the red PSD is already mitigated by a good 20-Hz editing procedure). Using the SARM and PLRM differences helped postprocess the latter to remove the main hump-generation events. If the hump still exists, then it is hidden by the large PLRM white noise.

With our editing parameters, approximately 20% of the PLRM dataset was edited out, and Fig. 18a shows that the edited measurements are aggregated in a number of small microsegments distributed along the track (i.e., neither a big corrupted block nor isolated outliers). Furthermore, it is generally difficult to find PLRM segments longer than a few hundreds of kilometers without any edited measurement: hump-generation events are local yet frequent.

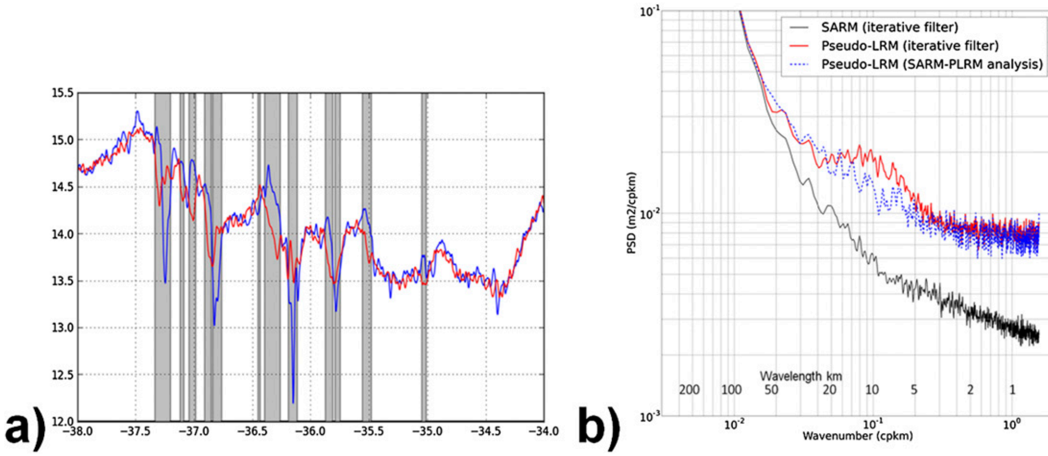

FIG. 18. (a) Concurrent measurements of SARM sigma0 (blue) and PLRM sigma0 (red) as a function of latitude for a 400-km segment of *Cryosat-2* track. (b) Mean PSD for SARM (black) and PLRM (red) SLA when the same nonlinear editing filter is used for both modes. The blue PSD from (b) is when PLRM minus SARM differences are used to detect and edit out the rapid changes in sigma0 that are observed differently by both modes [e.g., gray boxes in (a)].

These results not only confirm the findings from earlier sections but also highlight dual SARM/PLRM measurements from *Cryosat-2* as an attractive asset to design/validate new processing and postprocessing algorithms designed to mitigate LRM hump artifact.

The only limit of this approach is the white noise level of PLRM. Ideally, one would use SARM and LRM instead (not PLRM) to benefit from a low noise floor (to measure better the energy of the residual artifact or to confirm that it was removed), but this is not possible with altimeters from class *Cryosat-2* (or Sentinel-3).

3) IMPLICATIONS FOR SARM INSTRUMENTS, PROCESSORS, AND RESEARCH

Our findings illustrate the need to ensure the preservation and availability of high-level datasets for instrument and processing experts. For Jason-class missions, the 20-Hz rate is already available in the level 2 GDR and waveforms are distributed in the Sensor GDR. To that extent, LRM experts already have access to the data needed to carry out further investigations.

However, for *Cryosat-2* (or Sentinel-3) and SARM, there is a change of paradigm because there is level 1 processing step, namely, SAR stacking [described by Raney (1998) and implemented by Amarouche et al. (2013a) for Sentinel-3] that is not reversible. This emphasizes the new importance to preserve and to distribute level 1 SARM data to instrument processing experts because they will need such high-level data to develop and to validate better SARM algorithms in the future.

Furthermore, our LRM findings highlight a major caveat to SARM technology: 20 years after the first precise LRM altimeter missions, we are still investigating retracker-related errors and limitations of recent versions of the Brown model. It is therefore possible—if not likely—that the first generations of SARM retrackers are affected by similar flaws that were not yet detected with the limited SARM ocean coverage that *Cryosat-2* can provide.

This would advocate for larger SARM acquisitions (ideally basinwide or even global) from future SARM missions (e.g., Sentinel-3) and for the concurrent activation of the LRM and SARM with the so-called interleaved mode proposed for Jason Continuity of Service (Jason-CS; Phalippou et al. 2012) in place of the mutually exclusive LRM/SARM modes of *Cryosat-2* and Sentinel-3.

5. Conclusions

The observation of ocean scales smaller than 100 km with LRM altimetry products is degraded by the existence of a ‘‘hump artifact’’ visible on SSH spectra, that is, a spatially coherent error.

Through an analysis of simulations and actual data from multiple missions, we have shown that the hump originates in a response to inhomogeneities in backscatter strength (e.g., due to rapid changes of backscatter power induced by atmospheric and/or surface events). Current retrackers cannot fit their Brown model properly because they were designed for a scene with homogeneous backscatter properties. The error is also smoothed along track because of the size and shape of the LRM disc-shaped footprint.

The hump phenomenon occurs in all regions, although it is more intense at low latitudes and in the Indian Ocean and western Pacific Ocean, where backscattering events are more frequent. The spectral hump was also shown to be a systematic altimeter response to random events. The response is also modulated by the instrument design and altitude (size of the disc/rings associated with each waveform gate) and by the retracker used.

Because of the random nature of the phenomenon, a large majority of long SSH segments are affected (e.g., hundreds to thousands of kilometers). However, within these long segments, the bulk of the artifact energy is contained in small subsets of data (e.g., less than 10%). Thus, oceanography users interested in small-scale SSH signals can mitigate the hump corruption by using better editing and postprocessing algorithms on the 20-Hz rate of current products.

Moreover, the thin stripe-shaped footprint of *Cryosat-2*'s synthetic aperture radar mode (SARM) is not affected by the hump artifact, thus improving the observation of topography features ranging from 30 to 100 km. The differences between SARM and pseudo-LRM sigma0 can also be used to detect major hump events on pseudo-LRM data, which might be an asset to design/validate a new generation of algorithms aimed at reducing the hump artifact on the existing LRM record.

Last, because we investigate this LRM artifact 20 years after the launch of TOPEX/Poseidon (T/P) and *ERS-1*, our study emphasizes that agencies and users should also be cautious because SARM is a new technology that is not yet mature, and it emphasizes the benefits of providing support and high-level data to instrument processing experts so that they can improve their understanding of SARM technology.

Acknowledgments. This work was carried out with support from CNES (TOSCA/SWOT proposal, and SI/AR support) using SARM simulators and data developed as a contribution to the Sentinel-3 Project from ESA. The authors thank the reviewers as well as Dr. Lee-Lueng Fu and Dr. Pierre-Yves Le Traon for their insightful contribution to this analysis, and Dr. Philip Callahan for his analysis of TOPEX spectra.

REFERENCES

Ablain, M., S. Philipps, N. Picot, and E. Bronner, 2010: Jason-2 global statistical assessment and cross-calibration with Jason-1. *Mar. Geod.,* **33** (Suppl.), 162–185, doi:10.1080/01490419.2010.487805.

Amarouche, L., P. Thibaut, O. Z. Zanife, J.-P. Dumont, P. Vincent, and N. Steunou, 2004: Improving the Jason-1 ground retracking to better account for attitude effects. *Mar. Geod.,* **27,** 171–197, doi:10.1080/01490410490465210.

——, J.-P. Dumont, and A. Vernier, 2013a: Sentinel-3 core PDGS instrument processing facility (IPF) implementation—Detailed processing model SRAL L1. ESA Doc., Reference S3IPF. DPM.005, 465 pp.

——, N. Tran, and S. Jourdain, 2013b: Surface topography mission (STM)—SRAL system performance simulator specification (SY-18). ESA Doc., Reference S3-RS-CLS-SY-00028, 228 pp.

Birol, F., M. Cancet, and C. Estournel, 2010: Aspects of the seasonal variability of the Northern Current (NW Mediterranean Sea) observed by altimetry. *J. Mar. Syst.,* **81,** 297–311, doi:10.1016/j.jmarsys.2010.01.005.

Bouffard, J., A. Pascual, S. Ruiz, Y. Faugère, and J. Tintoré, 2010: Coastal and mesoscale dynamics characterization using altimetry and gliders: A case study in the Balearic Sea. *J. Geophys. Res.,* **115,** C10029, doi:10.1029/2009JC006087.

Boy, F., J.-D. Desjonquères, and N. Picot, 2011: Cryosat processing prototype (CPP): LRM, TRK and SAR processing. *Ocean Surface Topography Science Team Meeting,* San Diego, CA, AVISO, 16 pp. [Available online at http://www.aviso.oceanobs.com/fileadmin/documents/OSTST/2011/oral/01_Wednesday/Splinter%201%20IP/06%20%20Boy%20CPP%20Presentation.pdf.]

——, T. Moreau, J.-D. Desjonquères, S. Labroue, N. Picot, J.-C. Poisson, and P. Thibaut, 2012: Cryosat processing prototype, LRM and SAR processing on CNES side. *Ocean Surface Topography Science Team Meeting,* Venice, Italy, AVISO, 136. [Available online at http://www.aviso.oceanobs.com/fileadmin/documents/OSTST/2012/oral/02_friday_28/02_instr_processing_II/02_IP2_Boy.pdf.]

Brown, G. S., 1977: The average impulse response of a rough surface and its application. *IEEE Trans. Antennas Propag.,* **25,** 67–74, doi:10.1109/TAP.1977.1141536.

Callahan, P., and K. Oslund, 2009: TOPEX RGDR '09 analysis. *Ocean Surface Topography Science Team Meeting,* Seattle, WA, AVISO, 27 pp. [Available online at http://www.aviso.oceanobs.com/fileadmin/documents/OSTST/2009/oral/Callahan%20analysis.pdf.]

Challenor, P. G., and M. A. Srokosz, 1989: The extraction of geophysical parameters from radar altimeter return from a nonlinear sea surface. *Mathematics in Remote Sensing: Based on the Proceedings of a Conference on Mathematics and Its Application in Remote Sensing Held at Danbury, Essex in May 1986,* S. R. Brooks, Ed., Institute of Mathematics and its Applications Conference Series, Vol. 21, Clarendon Press, 257–268.

Chelton, D. B., and M. G. Schlax, 2003: The accuracies of smoothed sea surface height fields constructed from tandem altimeter datasets. *J. Atmos. Oceanic Technol.,* **20,** 1276–1302, doi:10.1175/1520-0426(2003)020<1276:TAOSSS>2.0.CO;2.

——, J. C. Ries, B. J. Haines, L.-L. Fu, and P. S. Callahan, 2001: Satellite altimetry. *Satellite Altimetry and Earth Sciences: A Handbook of Techniques and applications,* L-L. Fu and A. Cazenave, Eds., International Geophysics Series, Vol. 69, Academic, 1–132.

Dibarboure, G., M.-I. Pujol, F. Briol, P.-Y. Le Traon, G. Larnicol, N. Picot, F. Mertz, and M. Ablain, 2011: Jason-2 in DUACS: Updated system description, first tandem results and impact on processing and products. *Mar. Geod.,* **34,** 214–241, doi:10.1080/01490419.2011.584826.

——, and Coauthors, 2012: Finding desirable orbit options for the ''extension of life'' phase of Jason-1. *Mar. Geod.,* **35** (Suppl.), 363–399, doi:10.1080/01490419.2012.717854.

Dorandeu, J., M. Ablain, and P.-Y. Le Traon, 2003: Reducing cross-track geoid gradient errors around TOPEX/Poseidon and Jason-1 nominal tracks: Application to calculation of sea level anomalies. *J. Atmos. Oceanic Technol.,* **20,** 1826–1838, doi:10.1175/1520-0426(2003)020<1826:RCGGEA>2.0.CO;2.

Dussurget, R., F. Birol, R. Morrow, and P. De Mey, 2011: Fine resolution altimetry data for a regional application in the Bay of Biscay. *Mar. Geod.,* **34,** 447–476, doi:10.1080/01490419.2011.584835.

Faugère, Y., J. Dorandeu, F. Lefevre, N. Picot, and P. Femenias, 2006: Envisat ocean altimetry performance assessment and cross-calibration. *Sensors,* **6,** 100–130, doi:10.3390/s6030100.

Gómez-Enri, J., S. Vignudelli, G. D. Quartly, C. P. Gommenginger, P. Cipollini, P. G. Challenor, and J. Benveniste, 2010: Modeling Envisat RA-2 waveforms in the coastal zone: Case study of calm water contamination. *IEEE Trans. Geosci. Remote Sens.,* **7,** 474–478, doi:10.1109/LGRS.2009.2039193.

Guymer, T. H., G. D. Quartly, and M. A. Srokosz, 1995: The effects of rain on ERS-1 radar altimeter data. *J. Atmos. Oceanic Technol.,* **12,** 1229–1247, doi:10.1175/1520-0426(1995)012<1229:TEOROR>2.0.CO;2.

Hayne, G. S., 1980: Radar altimeter mean return waveforms from near-normal-incidence ocean surface scattering. *IEEE Trans. Antennas Propag.,* **28,** 687–692, doi:10.1109/TAP.1980.1142398.

Kim, S. Y., and Coauthors, 2011: Mapping the U.S. West Coast surface circulation: A multiyear analysis of high-frequency radar observations. *J. Geophys. Res.,* **116,** C03011, doi:10.1029/2010JC006669.

Klein, P., B.-L. Hua, G. Lapeyre, X. Capet, S. Le Gentil, and H. Sasaki, 2008: Upper ocean turbulence from high-resolution 3D simulations. *J. Phys. Oceanogr.,* **38,** 1748–1763, doi:10.1175/2007JPO3773.1.

Labroue, S., F. Boy, N. Picot, M. Urvoy, and M. Ablain, 2012: First quality assessment of the CryoSat-2 altimetric system over ocean. *Adv. Space Res.,* **50,** 1030–1045, doi:10.1016/j.asr.2011.11.018.

Laxon, S., 1994: Sea ice altimeter processing scheme at the EODC. *Int. J. Remote Sens.,* **15,** 915–924, doi:10.1080/01431169408954124.

Le Traon, P.-Y., and G. Dibarboure, 2002: Velocity mapping capabilities of present and future altimeter missions: The role of high-frequency signals. *J. Atmos. Oceanic Technol.,* **19,** 2077–2087, doi:10.1175/1520-0426(2002)019<2077:VMCOPA>2.0.CO;2.

——, Y. Faugère, F. Hernandez, J. Dorandeu, F. Mertz, and M. Ablain, 2003: Can we merge *GEOSAT Follow-On* with TOPEX/POSEIDON and *ERS-2* for an improved description of the ocean circulation? *J. Atmos. Oceanic Technol.,* **20,** 889–895, doi:10.1175/1520-0426(2003)020<0889:CWMGFW>2.0.CO;2.

——, P. Klein, B. L. Hua, and G. Dibarboure, 2008: Do altimeter data agree with interior or surface quasi-geostrophic theory? *J. Phys. Oceanogr.,* **38,** 1137–1142, doi:10.1175/2007JPO3806.1.

Martin-Puig, C., J. Marquez, G. Ruffini, R. K. Raney, and J. Benveniste, 2008: SAR altimetry applications over water. *Second Int. Workshop on Advances in SAR Oceanography from Envisat and ERS missions (SEASAR 2008),* Frascati, Italy, ESA, 21 pp. [Available online at http://earth.esa.int/workshops/seasar2008/participants/101/pres_101_martinpuig.pdf.]

Mitchum, G. T., D. W. Hancock, G. S. Hayne, and D. C. Vandemark, 2004: Blooms of σ^0 in the TOPEX radar altimeter data. *J. Atmos. Oceanic Technol.,* **21,** 1232–1245, doi:10.1175/1520-0426(2004)021<1232:BOITTR>2.0.CO;2.

Ollivier, A., 2006: Nouvelle approche pour l'extraction de paramètres géophysiques à partir des mesures en altimétrie radar. Ph.D. thesis, Institut National Polytechnique de Grenoble, 192 pp. [Available online at http://tel.archives-ouvertes.fr/docs/00/20/44/75/PDF/ollivier.pdf.]

Phalippou, L., and V. Enjolras, 2007: Re-tracking of SAR altimeter ocean power-waveforms and related accuracies of the retrieved sea surface height, significant wave height and wind speed. *IEEE International Geoscience and Remote Sensing Symposium: IGARSS Barcelona 2007; Sensing and Understanding Our Planet,* IEEE, 3533–3536, doi:10.1109/IGARSS.2007.4423608.

——, and F. Demeestere, 2011: Accurate numerical forward model for optimal retracking of SIRAL2 SAR echoes over open ocean. *2011 Fall Meeting,* San Francisco, CA, Amer. Geophys. Union, Abstract C53F-05.

——, L. Rey, P. de Chateau-Thierry, E. Thouvenot, N. Steunou, C. Mavrocordatos, and R. Francis, 2001: Overview of the performances and tracking design of the SIRAL altimeter for the CryoSat mission. *2001 IEEE International Geoscience and Remote Sensing Proceedings,* Vol. 5, IEEE, 2025–2027.

——, E. Caubet, F. Demeestere, J. Richard, L. Rys, M. Deschaux-Beaume, R. Francis, and R. Cullen, 2012: Reaching sub-centimetre range noise on Jason-CS with the Poseidon-4 continuous SAR interleaved mode. *Ocean Surface Topography Science Team Meeting,* Venice, Italy, AVISO, 12 pp. [Available online at http://www.aviso.oceanobs.com/fileadmin/documents/OSTST/2012/oral/02_friday_28/05_instr_processing_IIb/05_IP2B_Phalippou.pdf.]

Quartly, G. D., 1998: Determination of oceanic rain rate and rain cell structure from altimeter waveform data. Part I: Theory. *J. Atmos. Oceanic Technol.,* **15,** 1361–1378, doi:10.1175/1520-0426(1998)015<1361:DOORRA>2.0.CO;2.

——, 2009a: Improving the intercalibration of σ^0 values for the Jason-1 and Jason-2 altimeters. *IEEE Geosci. Remote Sens. Lett.,* **6,** 538–542, doi:10.1109/LGRS.2009.2020921.

——, 2009b: Optimizing σ^0 information from the Jason-2 altimeter. *IEEE Geosci. Remote Sens. Lett.,* **6,** 398–402, doi:10.1109/LGRS.2009.2013973.

——, 2010: Improving the altimetric rain record from Jason-1 and Jason-2. *J. Geophys. Res.,* **115,** C03008, doi:10.1029/2009JC005670.

——, 2011: Development and implementation of the hyperbolic pretracker. National Oceanography Centre Rep. COASTALT2-EWP3-D33-v2, 29 pp. [Available online at http://nora.nerc.ac.uk/439826/1/COASTALT2-EWP3-D33-v2.pdf.]

——, T. H. Guymer, and M. A. Srokosz, 1996: The effects of rain on TOPEX radar altimeter data. *J. Atmos. Oceanic Technol.,* **13,** 1209–1229, doi:10.1175/1520-0426(1996)013<1209:TEOROT>2.0.CO;2.

——, M. A. Srokosz, and A. C. McMillan, 2001: Analyzing altimeter artifacts: Statistical properties of ocean waveforms. *J. Atmos. Oceanic Technol.,* **18,** 2074–2091, doi:10.1175/1520-0426(2001)018<2074:AAASPO>2.0.CO;2.

Raney, R. K., 1998: The delay/Doppler radar altimeter. *IEEE Trans. Geosci. Remote Sens.,* **36,** 1578–1588, doi:10.1109/36.718861.

Richman, J. G., B. K. Arbic, J. F. Shriver, E. J. Metzger, and A. J. Wallcraft, 2012: Inferring dynamics from the wavenumber spectra of an eddying global ocean model with embedded tides. *J. Geophys. Res.,* **117,** C12012, doi:10.1029/2012JC008364.

Rodriguez, E., P. Callahan, and T. Lungu, 2007: TOPEX and Jason retracking. *Ocean Surface Topography Science Team*

Meeting, Hobart, TAS, Australia, AVISO, 24 pp. [Available online at http://www.marine.csiro.au/conf/ostst/talks/WedPlen/ost07tj-retrk-psc+er-f2.ppt.]

Sandwell, D. T., and W. H. F. Smith, 2005: Retracking ERS-1 altimeter waveforms for optimal gravity field recovery. *Geophys. J. Int.,* **163,** 79–89, doi:10.1111/j.1365-246X.2005.02724.x.

——, E. Garcia, and W. H. F. Smith, 2012: A comparison of altimeter noise from double retracked Geosat, ERS-1, Envisat, CryoSat and Jason-1 data. *Ocean Surface Topography Science Team Meeting,* Venice, Italy, AVISO, 18 pp. [Available online at http://www.aviso.oceanobs.com/fileadmin/documents/OSTST/2012/oral/02_friday_28/05_instr_processing_IIb/01_IP2B_sandwell.pdf.]

Sasaki, H., and P. Klein, 2012: SSH wavenumber spectra in the North Pacific from a high-resolution realistic simulation. *J. Phys. Oceanogr.,* **42,** 1233–1241, doi:10.1175/JPO-D-11-0180.1.

Scott, R.-B., and F. Wang, 2005: Direct evidence of an oceanic inverse kinetic energy cascade from satellite altimetry. *J. Phys. Oceanogr.,* **35,** 1650–1666, doi:10.1175/JPO2771.1.

Thibaut, P., F. Ferreira, and P. Femenias, 2007: Sigma0 blooms in the ENVISAT radar altimeter data. *Proc. Envisat Symp. 2007,* Montreaux, Switzerland, ESA, 464304. [Available online at http://earth.esa.int/workshops/envisatsymposium/proceedings/sessions/2E3/464304th.pdf.]

——, J. C. Poisson, E. Bronner, and N. Picot, 2010: Relative performance of the MLE3 and MLE4 retracking algorithms on Jason-2 altimeter waveforms. *Mar. Geod.,* **33** (Suppl.), 317–335, doi:10.1080/01490419.2010.491033.

——, ——, A. Halimi, C. M. Y. Tourneret, F. Boy, and N. Picot, 2012: A review of retracking solutions for coastal altimeter waveforms. *Fifth Coastal Altimetry Workshop,* San Diego, CA, National Oceanography Centre, 35 pp. [Available online at http://www.coastalt.eu/files/sandiegoworkshop11/pres/12_Thibaut_CLS_Retracking_Review.pdf.]

Tournadre, J., 1998: Determination of rain cell characteristics from the analysis of TOPEX altimeter echo waveforms. *J. Atmos. Oceanic Technol.,* **15,** 387–406, doi:10.1175/1520-0426(1998)015<0387:DORCCF>2.0.CO;2.

——, 2007: Signature of lighthouses, ships, and small islands in altimeter waveforms. *J. Atmos. Oceanic Technol.,* **24,** 1143–1149, doi:10.1175/JTECH2030.1.

——, B. Chapron, N. Reul, and D. C. Vandemark, 2006: A satellite altimeter model for ocean slick detection. *J. Geophys. Res.,* **111,** C04004, doi:10.1029/2005JC003109.

——, K. Whitmer, and F. Girard-Ardhuin, 2008: Iceberg detection in open water by altimeter waveform analysis. *J. Geophys. Res.,* **113,** C08040, doi:10.1029/2007JC004587.

——, J. Lambin-Artru, and N. Steunou, 2009: Cloud and rain effects on AltiKa/SARAL Ka-band radar altimeter—Part II: Definition of a rain/cloud flag. *IEEE Trans. Geosci. Remote Sens.,* **47,** 1818–1826, doi:10.1109/TGRS.2008.2010127.

Tran, N., E. Obligis, and F. Ferreira, 2005: Comparison of two *Jason-1* altimeter precipitation detection algorithms with rain estimates from the TRMM Microwave Imager. *J. Atmos. Oceanic Technol.* **22,** 782–794, doi:10.1175/JTECH1742.1.

Wingham, D. J., and D. W. Wallis, 2010: The rough surface impulse response of a pulse-limited altimeter with an elliptical antenna pattern. *IEEE Antennas Wireless Propag. Lett.,* **9,** 232–235, doi:10.1109/LAWP.2010.2046471.

Xu, Y., and L.-L. Fu, 2012: The effects of altimeter instrument noise on the estimation of the wavenumber spectrum of sea surface height. *J. Phys. Oceanogr.,* **42,** 2229–2233, doi:10.1175/JPO-D-12-0106.1.

Zanife, O. Z., P. Vincent, L. Amarouche, J. P. Dumont, P. Thibaut, and S. Labroue, 2003: Comparison of the Ku-band range noise level and the relative sea-state bias of the Jason-1, TOPEX, and Poseidon-1 radar altimeters. *Mar. Geod.,* **26,** 201–238, doi:10.1080/714044519.